Occurrence of ice-rafted erratics and the petrology of the KR1 seamount trail from the Australian–Antarctic Ridge

Article *in* International Geology Review · June 2019

DOI: 10.1080/00206814.2018.1514669

6 authors, including:

Sang-Bong Yi
Korea Polar Research Institute
12 PUBLICATIONS **90** CITATIONS

Sung-Hyun Park
Korea Polar Research Institute
30 PUBLICATIONS **470** CITATIONS

Seunghee Han
Korea Polar Research Institute
4 PUBLICATIONS **9** CITATIONS

Hakkyum Choi
Korea Polar Research Institute
10 PUBLICATIONS **30** CITATIONS

Title

Occurrence of ice-rafted erratics and the petrology of the KR1 seamount trail from the Australian–Antarctic Ridge

Authors

Sang-Bong Yi, Mi Jung Lee *, Sung-Hyun Park, Seunghee Han, Yun Seok Yang, Hakkyum Choi

Division of Polar Earth-System Sciences, Korea Polar Research Institute, Incheon 21990, Republic of Korea

Sang-Bong Yi

E-mail address: handjive@kopri.re.kr

Mi Jung Lee * [*Corresponding author]

E-mail address: mjlee@kopri.re.kr

Division of Polar Earth-System Sciences, Korea Polar Research Institute, Songdomirae-ro 26, Yeonsu-gu, Incheon 21990, Republic of Korea

Abstract

A multi-disciplinary study of the KR1 segment of the Australian-Antarctic Ridge has been conducted since 2011. We present geochemical and age dating results for samples dredged from three sites on the KR1 seamount trail. The majority of the samples are alkaline ocean island basalts with subdominant enriched tholeiites. The samples from the DG05 bathymetric depression include ice-rafted erratics from Antarctica, which consist of gabbro, diabase, various granitoids, volcanic rocks such as trachyte and rhyolite and deformed or undeformed

sedimentary rocks. The main provenance of glacial erratics is considered to be the the Ross Sea region. However, Carboniferous to Cretaceous ages of erratics indicate that some of these may originate from the western regions of West Antarctica. Based on the size and topography of the volcanic features and geochemical characteristics of the alkaline ocean island basalts (La/Sm_N = 2.62–3.88; Tb/Yb_N = 1.54–2.67) and the enriched tholeiites, the KR1 seamount trail is interpreted to be a submarine hotspot chain that is the product of alkaline volcanic eruption and seafloor spreading.

Keywords: Australian-Antarctic Ridge; KR1 seamount trail; ocean island basalt; glacial erratics; Antarctica

1. Introduction

Oceanic crust is composed of several layers including the uppermost basaltic pillow lavas underlain by feeder or sheeted dikes and mafic plutonic rocks such as diabase or gabbro. Due to the thickness of the uppermost basaltic layer, the lower plutonic rocks are rarely sampled at the ocean floor. However, they have been sampled together with oceanic granites or ultramafic rocks at slow- to ultraslow-spreading mid-ocean ridges (MOR; e.g., the Central Indian Ridge, Southwest Indian Ridge and Mid Atlantic Ridge), where they are exposed as a result of detachment faults associated with rifting that tilts and exposes deeper oceanic crust as well as mantle (e.g., Cannat et al., 1995; Dick et al., 2003; Ildefonse et al., 2007 ; Sauter and Cannat, 2010; Tucholke et al., 2008; Yi et al., 2014;).

Unlike this kind of structurally exposed rocks, ice-rafted continental clasts have been reported in the Arctic and Southern ocean floors (e.g., Andrews, 2000; Barret et al., 1975; Bischof, 2000; Dowdeswell et al., 1995; Gilbert, 1990). These sediments are good indicators to interpret the ocean environment and continental subglacial geology, especially in Antarctica, where most of the surface is covered by glaciers. However, when ice-rafted clasts are deposited over in situ bedrock, it can be difficult to interpret the underlying geology correctly. As a result, one of the issues for ocean floor research is finding suitable discrimination criteria to distinguish between glacial erratics and bedrock consisting of variable geology.

Seamounts are submarine volcanoes of varying sizes, ranging in height from 50–100 m to over 1500 m above the surrounding ocean floor, that have a variety of origins. They can form near the MOR, as intraplate hotspot tracks and in convergent island arc tectonic settings (Staudigel and Clague, 2010; Wessel et al., 2010). Thus, the interpretation of seamount formation should be considered in the context of their geomorphology, size and tectonic setting.

The present study investigates the formation process of a series of seamounts (the KR1 seamount trail) that developed parallel to the spreading directions of the Australian-Antarctic Ridge, which is also known as the Southeast Indian Ridge (Figure 1). Glassy olivine basalts and tholeiitic basalts are found along the KR1 seamount trail. In a bathymetric depression, which is interpreted to be a crater, various types of gravel clasts were found in addition to oceanic basalts. These gravel clasts consist of mafic plutonic rocks, granitoids and various volcanic and sedimentary rocks, which are more rounded than oceanic basalts. Some of the clasts have faceted surfaces suggestive of glacial abrasion, which suggests that they are not part of the oceanic crust, but ice-rafted glacial sediments transported from Antarctica.

This paper is arranged as follows: first the rocks recovered from the KR1 seamount trail are classified. Then, the origin of the ice-rafted clasts found in the bathymetric depression is determined using age and geochemical data. Finally the formation process of the KR1 seamount trail is discussed based on its geomorphology and geochemical characteristics of the basalts.

2. Geological setting and the dredged site

The study area of the KR1 segment of the eastern part of Australian-Antarctic Ridge in the Southern Ocean is part of an ongoing series of multi-disciplinary studies on the KR1, KR2 and KR3 segments that has been undertaken by the Korea Polar Research Institute (KOPRI) since 2011. A series of bathymetric surveys and rock sample dredgings around the KR1 spreading ridge and its vicinity were carried out by KOPRI's icebreaker R/V *Araon* in 2013. The KR1 segment connects the Australian-Antarctic Ridge with the Pacific-Antarctic Ridge and the Hjort Trench at the Macquarie Triple Junction (Figure 1a). Choi et al. (2017) report that the full spreading rate of the KR1 segment is 63–66 mm/yr.

The general bathymetry along the KR1 spreading centre (on-axis) varies from 2800 m below sea level (bsl) in the northeast of the study area to around 1850 m bsl in the vicinity of the KR1 seamount trail and 1750 m bsl in the southwest of the study area on another seamount. Outside the spreading centre water depths increase towards the southeast and northwest. The spreading centre is recognized as an area of reduced seabed depths with water depths increasing gradually away from the spreading centre (Figure 1b). Around the KR1 spreading ridge, there are a number of isolated and linear seamounts reaching heights of over 1000 m above the surrounding seabed. Of these, the KR1 seamount trail is a series of large-scale bathymetric highs that reach up to 1600m above the ocean floor (Figure 1c), and extend to the southeast, parallel to the spreading direction. The elevation of the KR1 seamount trail is the highest in the 1080 summit (c. 1080 m bsl), which is 20-25 km away from the spreading centre, and decreases away from it to the spreading direction. The KR1 seamount trail ends approximately 60 km away from the spreading axis.

Samples were collected from three dredge sites (DG05, DG04 and DG03) along the KR1 seamount trail (Figure 1c). The DG05 area (c. 1650 m bsl) is interpreted as a volcanic crater based on a topographic low seen in the bathymetric data. A large tholeiitic basalt with a volume of c. 52,000 cm^3 (c. 43 cm in length) and an olivine basalt with a volume of c. 2,000 cm^3 (c. 20 cm in length) were recovered along with rounded or subrounded gravels including mafic plutonic rocks, granitoids and various volcanic and sedimentary rock clasts (5–10 cm in length; Supplementary Figures 1a, 1b, and 2). The DG04 area (c. 1390 m bsl), the shallowest of the dredge sites, included the summit of a seamount and the surrounding areas. The recovered samples here include four olivine basalts with lengths of approximately 3 cm (Supplementary Figure 1c). The rocks recovered from the DG03 area (c. 1560 m bsl), located near the summit of a seamount at south-eastern end of the seamount trail, include three olivine basalts, two tholeiitic basalts and one tuff, that have lengths of approximately 5 cm (Supplementary Figure 1d). In summary, the surface of the KR1 seamount trail consists mainly of olivine basalts (alkali basalts) and tholeiitic basalts, and various types of clasts cover a surface of the DG05 depression (Figure 1c).

3. Analytical methods

Whole-rock analyses were made on fresh samples leached in a dilute acid solution. The samples were pulverized to <150 mesh (105 μm) powder in a tungsten carbide mill bowl (Ni and Cr-free). Major element concentrations were determined by X-ray fluorescence (XRF) spectrometry using a PANanalytical Axios Max at KOPRI. The detailed analysis procedure follows the description from Mori and Mashima (2005).

For whole-rock trace element analyses powdered rock samples were dissolved in HF and $HClO_4$ acids. The solutions were analyzed at KOPRI using an inductively coupled plasma mass spectrometer (ICP-MS; Thermo iCAP Q), and the mean value of three separate analyses were used. For quality control, certified reference materials (BCR-2 and JG-3) were analyzed with the unknown samples, and replicate analyses for two unknown samples (DG03-1 and DG05-1C) were performed. The analytical errors in the reference materials were within 10% of the known values, and the errors in the replication analyses were within 3%.

The major element concentrations of the basalt glasses were analyzed using a JEOL JXA-8530F field emission (FE) electron probe micro-analyzer (EPMA) at KOPRI using a 15 kV accelerating voltage, 10 nA beam current and a probe diameter of 10 μm to reduce alkali loss. For Na_2O and K_2O, the peak and background count times were 10 s and 5 s, respectively. For other oxides the peak and background times were 20 s and 10 s, respectively. Certified natural basalt glasses and synthetic oxide were used as standards, and the natural basalt glasses include GSE-1G, BCR-2G and BIR-1G. The probe data were processed using the conventional PRZ.

Conventional K-Ar age dates of volcanic rocks were made on fresh groundmass materials after phenocrysts were removed. The K concentration was measured using a Unicam 989 atomic absorption spectrometer, and the Ar isotope composition was measured using a VF5400 static vacuum mass spectrometer. Analyses were conducted in the Ochang Centre of the Korea Basic Science Institute (KBSI). The isotope ratios of Ar were calibrated using the discrimination factor, which is based on standard air contents. The content and error calculations of the radiogenic ^{40}Ar followed the procedure of Nagao et al. (1996). During the analysis, the hot blank level of ^{40}Ar was less than 2.0×10^{-9} cm^3 STP, and the Ar isotope ratios in the blank run were the same as the atmospheric Ar isotope ratios within the analytical error limits. The detailed analysis procedures can be found in Kim (2001).

U-Pb age determination of zircon was performed by in situ laser ablation multi-collector (LA-MC)-ICPMS at the Ochang Centre of KBSI. In situ analyses were performed using a NWR193^{UC} (ESI) laser ablation system coupled to a Nu Plasma II MC-ICPMS with the collector configured for simultaneous measurements of Th, U, Pb and Hg isotopes. The ablation was conducted on a spot of 15 μm in size, at a frequency of 5 Hz and at a fluence of 4~7 J/cm^3.

The ablation material was carried by Ar (~0.7 L/min) and He (~0.6 L/min). Background intensities, dwell time and wash out time were measured at 30, 30 and 15 s, respectively. Analysis was conducted using the time resolved analysis mode of the Nu Plasma software, and signals were integrated, which excludes the first 2-5 s of data. The data normalizing and uncertainty propagation was performed using Iolite 2.5 software (Paton et al., 2011). For every standard and sample set, measurements and blank values were collected under the same conditions, and the values were subtracted from all individual cycle measurements. A sample-standard bracketing technique was adopted to correct for the minute change in the ion counter. During each analytical session, a reference zircon was measured between each group of five unknown spot analyses to determine the inter-elemental fractionation and instrumental mass discrimination. Zircon 91500 was used as the primary reference (1062 ± 0.4 Ma; Wiedenbeck et al., 1995) and Plesovice zircon was used as a secondary reference (337.1 ± 0.4 Ma; Slama et al., 2008). All plots and age calculations were made using Isoplot 3.71 (Ludwig, 2003).

4. Petrography

Olivine basalts were found at all three dredge sites, and tholeiitic basalts occur in the DG03 and DG05 dredges (Supplementary Figure 1). A variety of rock clasts are found with the basalts at the deepest site (DG05 area). Non-basaltic rocks recovered from the DG05 area are rounded or subrounded clasts, and include mafic plutonic rocks (e.g., gabbro and diabase), various granitoids, volcanic rocks (e.g., rhyolite and trachyte) and deformed or undeformed sedimentary rocks (e.g., greywacke and sandstone) (Supplementary Figure 2).

The basaltic rocks in this study are classified into two types: 1) tholeiitic basalts ranging from aphyric to porphyritic in texture with plagioclase microphenocrysts and 2) olivine basalts with phaneritic olivine phenocrysts. The tholeiitic basalt (sample DG05-1) has an elliptical two-dimensional shape, and is derived from a pillow lava with a glass crust. The presence of iron hydroxide–manganese oxide on the separated surface implies that this sample is a boulder detached from the parent body prior to dredging (Supplementary Figure 1a). The microcrystalline olivine basalt (sample DG05A) is holocrystalline without a glass crust and has an angular morphology, which may indicate that this sample was initially located under the uppermost basalt layer and separated from its original position prior to falling into the crater due to gravity (Supplementary Figure 1b).

Tholeiitic basalts have a glass crust with approximately 1 mm thick manganese oxide developed on the outer edge due to reaction with seawater. They have weakly developed medium-grained phenocrysts and mainly contain plagioclase and clinopyroxene microphenocrysts. Plagioclase microphenocrysts occur mainly in the form of elongated needle. Olivine occurs mainly as a skeletal grain that is smaller than plagioclase and clinopyroxene microphenocrysts. Backscattered electron (BSE) images of the cryptocrystalline groundmass show it is predominantly composed of dendritic pyroxene and plagioclase aggregates. The clinopyroxene–plagioclase crystallites, which are mainly composed of cryptocrystalline plagioclase–clinopyroxene crystals surrounding plagioclase cores, which form nodules of approximately 100 μm in diameters, are well developed in the transition zone between the glass and crystalline components (Figures 2a and b). The textures are indicative of quenching of the tholeiitic basalts.

The olivine basalts are characterized by medium-grained olivine phenocrysts or olivine microphenocrysts. Many olivine phenocrysts host melt and chromian spinel inclusions. Plagioclase and clinopyroxene are present together as microphenocrysts. The groundmass is cryptocrystalline or microcrystalline, and consists mainly of clinopyroxene, plagioclase and opaque minerals. Some olivine basalt samples exhibit a flow texture with weakly aligned plagioclase laths in one direction. The outermost part of the olivine basalt glass is coated with manganese oxide, which developed to a 1 mm thickness and indicates the reaction of basalt and seawater. In the glass portion, crystallites consisting of dendritic plagioclase–clinopyroxene aggregate occur together with skeletal olivine grains, which indicate a quenching texture (Figures 2c–f).

5. Whole-rock geochemistry

Whole-rock major and trace element analyses of the basaltic rocks and various clasts are listed in Supplementary Table 1. The basalts are classified into alkaline and subalkaline basalts on the total alkaline *versus* silica (TAS) diagram (Figure 3a). In the K_2O *versus* silica diagram, the alkaline basalts correspond to the medium-K or the shoshonitic series, and the subalkaline basalts (tholeiites) correspond to the low-K tholeiite series (Figure 3b). Olivine basalts are chemically equivalent to alkaline basalts (hereafter alkali basalts). According to the trace element concentrations in the Nb/Y *versus* $Zr/P_2O_5 \times 10^4$ diagram, the alkali basalts found in the study area are typical of oceanic alkali basalt, and the tholeiitic basalts are similar to oceanic tholeiite (Figure 3c). In the tectonic discrimination diagram, the alkali basalts are consistent with intra-plate alkali basalts, and the tholeiites mostly plot in the enriched-mid ocean ridge basalt (E-MORB) field, except for one sample (Figure 3d).

On the chondrite-normalized rare earth element (REE) diagram and the normal-MORB (N-MORB)-normalized multi-element variation diagram, the alkali basalts show a pattern similar to ocean island basalt (OIB) which are enriched with light REEs (LREE; La/Sm_N = 2.62–3.88), large ion lithophile elements (LILE: Rb, Ba, K and Sr) and high field strength elements (HFSE: Th, U, Nb, Zr and Ti; Figures 4a and b). The tholeiites, in contrast, have similar REE abundances (La/Sm_N = 1.22–1.33) to E-MORB or transitional-MORB (T-MORB). However, the trace element abundances are similar to E-MORB in the multi-elemental variation diagram

(Figures 4c and d).

The various clasts recovered in the DG05 dredge include a gabbroic rock (DG05W), which plots as a subalkaline gabbroic diorite in the TAS diagram (Figure 3a). The granite clast (DG05S) is subalkaline, and the other three granitoid clasts (DG05J, DG05I and DG05R) have transitional characteristics akin to the alkaline series. Two samples of volcanic rock clasts belong to alkaline trachyte (DG05X) and subalkaline rhyolite (DG05O), respectively (Figure 3a). The clasts have distinct geochemical characteristics that relate to different series in the TAS diagram, as well as in the K_2O *versus* silica diagram (Figure 3b). In the tectonic discrimination diagram, the trace element content of the gabbroic diorite is similar to those of volcanic arc basalts or intra-plate tholeiites. Moreover, the granitoids plot in the area of volcanic arc granites and collision-related granites (Figures 3c and d).

On the chondrite-normalized REE diagram, the gabbroic diorite exhibits a slightly enriched LREE and flat heavy REE (HREE) pattern. In the N-MORB-normalized multi-element variation diagram, the gabbroic diorite exhibits a pattern with Nb–Ta–P–Ti troughs and K–Pb positive spikes, which shows typical characteristics of volcanic arc mafic magmatism (Figures 5a and b). Various granitoid clasts have similar LREE contents, but differing HREE contents. In the multi-elemental variation diagram, the granitoid Rb, Ta, and Nd contents differ (Figures 5c and d). The rhyolite has strongly enriched LREE contents in the chondrite-normalized REE diagram. The HREEs Ho, Tm and Yb are below the detection limit, which is possibly due to leaching by seawater. In the multi-elemental variation diagram, the rhyolite shows troughs for the Ta–Nb–P–Ti contents and positive spikes for the K–Pb contents. This aspect is similar in the trachyte sample, which possibly indicates that these are volcanic arc igneous rocks formed in subduction environments (Figures 5e and f).

Taken together, the various igneous rock clasts dredged in the DG05 area represent different geochemical sequences and have geochemical characteristics related to magmatic arc and continental collision. This suggests that they are unlikely to be oceanic in nature and supports the thesis that they are exotic materials.

6. Geochronology

6.1. K–Ar ages of basalts and other volcanic rock clasts

Five samples were selected for whole-rock K-Ar age dating: two alkali basalts (DG04-2 and DG05A), one tholeiite (DG05-1C), one rhyolite clast (DG05O), and one trachyte clast (DG05X) (Supplementary Figures 1 and 2). The analytical results are listed in Supplementary Table 2.

The K–Ar age of one of the alkali basalt sample (DG04-2) is 4.6 ± 0.7 Ma, which is somewhat older than the age predicted by the magnetic anomaly of ocean floor basalt (c. 1 Ma; Choi et al., 2017) and suggests the sample may contain excess ^{40}Ar. The K–Ar ages of DG05A (alkali basalt) and DG05-1C (tholeiite) are 11.2 ± 0.7 Ma and 17.2 ± 0.7 Ma, respectively. The ages are older than the predicted ocean floor age and, once again, it implies that the samples contain excess ^{40}Ar. The cause of excess argon in submarine basalts has been described in many papers (e.g., Dalrymple, 1969; Dalrymple and Moore, 1968; Fisher, 1981; Ozima et al., 1977; Seidemann, 1977). Dalrymple and Moore (1968) noted that excess ^{40}Ar occurs in glassy submarine basalts which formed by quenching under hydrostatic pressure. The excess ^{40}Ar which exists in the mantle source dissolves in the magma but cannot be degassed during eruption due to the pressure of the overlying sea water. Thus, the K–Ar age for submarine basalts can be older than their actual age. The presence of excess ^{40}Ar in the mantle (i.e., initial argon prior to the source mantle-melting event) is identified in the high $^{40}Ar/^{36}Ar$ ratios in the upper and lower mantles (see Burnard et al., 1997; Graham, 2002; Moriera et al., 1998).

The two volcanic rock clasts dredged from the DG05 depression yield ages of 291.6 ± 5.5

Ma (DG05O, rhyolite) and 150.9 ± 3.3 Ma (DG05X, trachyte), which are significantly older than the age of oceanic crust adjacent to the MOR and their sample location. This confirms that the two volcanic clasts are exotic materials derived from within a continent

6.2. Zircon U–Pb ages of plutonic rock clasts

One gabbroic rock and three granitoid clasts were selected for zircon U-Pb age dating using LA-MC-ICPMS. The analytical results are listed in Supplementary Table 3, and the concordia diagram for the zircon U–Pb data are shown in Figure 6.

Zircons from the gabbroic diorite (DG05W) are generally stubby prismatic grains, and several grains are subrounded. The grain size ranges from 30 to 80 μm in lengths with aspect ratios of 1.2 to 2.0. The grains exhibit concentric zoning in the cathodoluminescence (CL) images and have Th/U values of 0.37–0.81. Eleven spots on the magmatic zircons yield a weighted mean $^{206}Pb/^{238}U$ age of 336.2 ± 1.8 Ma (MSWD = 0.69; Figure 6a). Zircons from the granodiorite (DG05R) are mostly prismatic, with lengths of 50–200 μm and aspect ratios of 1.5–3.0. The grains show concentric zoning in the CL images. Though several isotope values related to common lead contents plot in discordant positions on the concordia diagram, ten spots (Th/U = 0.77–1.72) are concordant and yield a weighted mean $^{206}Pb/^{238}U$ age of 100.4 ± 0.5 Ma (MSWD = 0.64; Figure 6b). Zircon grains from the granite (DG05H) are generally stubby prismatic, with lengths of 50–150 μm and aspect ratios of 1.2–2.5. The grains exhibit concentric zoning in the CL and have Th/U values of 0.37–0.81. Isotope values of fifteen spots plot in concordant positions in the diagram and yield a weighted mean $^{206}Pb/^{238}U$ age of 298.4 ± 1.2 Ma (MSWD = 0.53; Figure 6c). Zircons from the granite (DG05I) are mostly stubby prismatic grains with lengths of 60–200 μm and aspect ratios of 1.2–2.5. The grains exhibit concentric zoning in the CL and have Th/U values of 0.58–1.56. Four spots related to common lead contents are discordant in the concordia diagram but sixteen spots yield a weighted mean $^{206}Pb/^{238}U$ age of 228.8 ± 0.5 Ma (MSWD = 1.02; Figure 6d).

The four plutonic rock clasts are of different igneous ages: Carboniferous (336.2 ± 1.8 Ma), Permian (298.4 ± 1.2 Ma), Triassic (228.8 ± 0.5 Ma) and Cretaceous (100.4 ± 0.5 Ma). Considering these ages and the geochemical evidences, these clasts all correspond to igneous rocks formed within a continent.

7. Discussion

7.1. Formation of the KR1 seamount trail

The composition of oceanic basalts is determined by various factors such as the source mantle composition, the depth and degree of partial melting and the volatile phases involved. Alkaline basaltic magma is considered to form preferentially in conditions of relatively high fertility of the source material, high pressure melting conditions, low partial melt fraction and CO_2-rich volatile involvement (Eggler, 1974; Finn et al., 2005; Kinzler and Grove, 1993; Kushiro, 1996 and 2001). The complexity of the origin of these alkali basalts has led to diverse views on the formation of OIB, seamount volcanic rocks and enriched tholeiites (i.e., E-MORBs), as well as their interrelations (e.g., Anderson, 2006; Fitton, 2007; Niu et al., 2002; Niu and Batiza, 1997; Phipps Morgan, 1999; Yamamoto et al., 2007). Alkali basalts on the ocean floor are mainly considered to be the result of: 1) the partial melting of relatively primordial mantle or recycled oceanic lithosphere with mantle associated with a mantle plume; 2) off-axis magmatism in a divergent tectonic setting with low melt fraction; 3) the partial melting of fertile blobs from oceanic or continental lithosphere with additional depleted upper mantle and 4) a combination of these processes (e.g., Ballmer et al., 2013; Bourdon et al., 1996; Koppers, 2011; Niu et al., 2002; Phipps Morgan and Morgan, 1999; Vlastelic and Dosso, 2005).

The KR1 seamount trail is a series of volcanoes on the ocean floor that developed parallel to one of the spreading directions (SE direction) of the MOR. The length of the seamount trail is approximately 60 km, and the maximum height is about 1600 m above the ocean floor (Figures 1b and c). The constituent rocks are mostly alkali basalts with subdominant enriched tholeiites. The alkali basalts in the study area are similar to the OIB, which is characterized by enrichments of LREE, LILE (such as Rb, Ba, K and Sr) and HFS (Figure 4). Although an in-depth discussion on the origin of these alkali basalts is difficult without an isotopic data, the HREE abundance of the basalts indirectly implies that these two basalts have different origins (Figure 7). It is notable that the alkali basalts (Tb/Yb_N = 1.54–2.67) and tholeiites (Tb/Yb_N = 1.16–1.33) are differentiated with different source areas and that the alkali basalts have a closer garnet-affinity in source material composition than the tholeiites. This supports the possibility that the alkali basalts and tholeiites originate from different sources and that the source of the alkali basalts is more deeply rooted than that of the tholeiites.

The occurrence of the enriched tholeiites, together with the alkali basalts has important implications for the KR1 seamount trail formation. It is necessary to interpret whether the tholeiites are part of the uplifted ocean floor that migrated by seafloor spreading after being formed in the MOR, or the incipient product related to alkaline magmatism that occurred away from the MOR. With regard to the development of an ocean island, the submarine shield is formed first and consists of enriched tholeiites, and then the island is created by the eruption of alkali basalt (Fitton, 2007; Frey et al., 2005; Garcia et al., 1995; Regelous et al., 2003). The KR1 seamount trail may have an eruption history similar to that of the papers cited above, where the tholeiite is the first to erupt and the alkali basalt erupts later.

There are a number of submarine volcanoes over 1000 m high, some of which appear near the MOR axis (Figure 1a). The highest seamount in the area is located within the KR1 seamount trail, as is MOR along-axis elevation, which decreases toward the periphery. This suggests that the KR1 seamount trail, with or without the large seamounts, may be the result of independent mantle upwelling distinct from the MOR magmatism. The conclusion on whether the KR1 seamount trail was formed as a result of a deep mantle upwelling, deeper than upper mantle convection attributed to MORB formation, or the volcanic chain originating from a shallow source (upper mantle with fertile blobs) can be completed by whole-rock isotope research and seismic tomography of the mantle structure.

The term of 'hotspot' has mainly been used to describe the volcanic output of a mantle plume (Fitton et al., 1997; Hannan and Schilling, 1997; Morgan, 1971; White and Duncan, 1993). However, the results of geological surveys over the last 20 years have shown that there are various types of alkaline seamounts, seamount trails and ocean islands in addition to Morgan-style hotspots, and some of which are still named 'hotspot' (e.g., Hirano et al., 2006; Kopper, 2011; McNutt, 2006). Considering the scale and linear geomorphology of the volcanic chain and the occurrence of alkali basalt, the KR1 seamount trail is likely to be a submarine hotspot trail.

The eruption timing of the KR1 seamount trail can be indirectly estimated from the magnetic anomaly ages of the ocean floor. The KR1 seamount trail is interpreted to be younger than 1.8 Ma because the magnetic anomaly age of the ocean floor near the outermost part of the KR1 seamount trail is estimated at approximately 1.8 Ma (Choi et al., 2017). In addition, since the formation age of the ocean floor near the 1080 summit, which is the highest summit of the KR1 seamount trail, is inferred to be 0.78 Ma (Choi et al., 2017), the formation and volcanic eruption of the 1080 summit can be interpreted as occurring after 0.78 Ma (Figure 1c). However, the conclusion about whether the linear KR1 seamount trail was formed by seafloor spreading with a single eruption vent or by several eruption vents is unclear in the present data. The formation and development of the KR1 seamount trail can be specified through precise age dating.

7.2. The origin of diverse clasts in the DG05 dredge

The exotic clasts in the DG05 dredge consist of mafic plutonic rocks, granitoids and various volcanic and sedimentary rocks (Supplementary Figure 2). These clasts are considered to be ice-rafted materials from Antarctica based on the following reasoning. The circulation pattern of sea ice and the direction of the ocean surface current around Antarctica show that the study area lies within the area of influence of the Antarctic icebergs, many of which are derived from the Ross Sea (Figure 8a). The crater-like depression of the DG05 area has geographical and topographical features that can accommodate large quantities of glacial debris originating from Antarctica, especially those flowing through the Ross Sea. Analysis of the drainage basins of Antarctic ice sheets demonstrates that the provenance of the diverse erratics found in the DG05 depression is a somewhat limited area, as shown in Figure 8a. The area is mainly confined to Victoria Land, the central Transantarctic Mountains, Marie Byrd Land and inland of East Antarctica.

Antarctic rocks vary in age from Archean to Phanerozoic. The continental side of the Transantarctic Mountains (i.e., inland of East Antarctica) is composed of old rocks of Archean to Proterozoic ages (Boger, 2011; Fitzsimons, 2000; Harley and Kelly, 2007; Jacobs, 2009). The Pacific side of the Transantarctic Mountains and West Antarctica correspond to the Phanerozoic continental margin that was completed by crustal accretion and arc magmatism (Figure 8b) (Boger, 2011 and references therein; Cawood, 2005). The Pacific side of the Transantarctic Mountains corresponds to the passive margin of the Gondwana plate margin and has experienced crustal accretion, magmatism and metamorphism by arc orogeny (i.e., Ross orogeny) in the early Paleozoic (Boger, 2011; Boger et al., 2001; Elliot, 2013; Rocchi et al., 2011). This aspect of arc orogeny extended to the Devonian–Carboniferous period and led to the growth of West Antarctica. Subduction-related crustal accretion and magmatism influenced all of West Antarctica, including the Antarctic Peninsula, from the late Paleozoic to the Mesozoic, and the major magmatic episodes are summarized in late Triassic to early Jurassic (235–200 Ma), mid-Jurassic (~180–160 Ma) and early to late Cretaceous (~ 140–80 Ma) (Leat et al., 1995; Siddoway and Fanning, 2009; Storey et al., 1996). Apart from this aspect, early Jurassic volcanism (i.e., Ferra igneous group) associated with the breakup of Gondwana is reported in the west margin of East Antarctica, and the Cenozoic volcanism associated with the development of the West Antarctic rift is reported in the west margin of East Antarctica and West Antarctica (Elliot, 2013; Hart and Kyle, 1993; Rocchi et al., 2002; Storey et al., 2013).

The absence of Precambrian rocks in the age-determined clasts indicates that the studied glacial erratics more likely originated in Victoria Land, the central Transantarctic Mountains and Marie Byrd Land rather than in the East Antarctic inland (Figures 8a and b). Among the DG05 glacial erratics, deformed sedimentary rocks and undeformed volcanic rocks can be comparable to Paleozoic sedimentary rocks and Mesozoic to Cenozoic volcanic rocks in these areas, respectively. The determined formation ages of the DG05 glacial erratics are 336.2 ± 1.8 Ma (gabbroic diorite), 298.4 ± 1.2 Ma (granite), 291.6 ± 5.5 Ma (rhyolite), 228.8 ± 0.5 Ma (granite), 150.9 ± 3.3 Ma (trachyte) and 100.4 ± 0.5 Ma (granodiorite) (Figure 6 and Supplementary Tables 2 and 3). Rocks of similar ages to these erratics are identified in West Antarctica (i.e., Marie Byrd Land, Thurston Island and the Antarctic Peninsula) (Figures 8a and b). These areas, in particular, correspond to the Gondwana plate margin during the late Paleozoic to Mesozoic, and to various magmatic arcs developed during the Devonian to Cretaceous (Elliot, 2013 and references therein; Leat et al., 1995; Storey et al., 1996).

The Carboniferous gabbroic diorite (sample DG05W) is comparable with arc-type plutonic rocks identified in Marie Byrd Land, based on its trace element geochemistry (Figure 5). Late

Carboniferous to Permian plutonic rocks, similar to the granite sample DG05H are found in Marie Byrd Land, Thurston Island and on the Antarctic Peninsula (Elliot, 2013; Pankhust et al., 1998; Veevers and Saeed, 2011 and 2013). Early Permian volcanic rocks, similar to the rhyolite sample DG05O, have not yet been identified in outcrops within Antarctica. However, the existence of this volcanism can be deduced from early Permian detritus identified in the Triassic strata within the Transantarctic Basin and the early Permian quartz diorite found in Marie Byrd Land (Collinson et al., 1994; Veevers and Saeed, 2011). Triassic plutonic rocks, similar to the granite sample DG05I, have been identified on Thurston Island and on the Antarctic Peninsula. Middle and upper Jurassic volcanic rocks, similar to the trachyte sample DG05X, are mainly found on the Antarctic Peninsula (Elliot, 2013; Veevers and Saeed, 2011, 2013; Pankhust et al., 2000), yet this trachyte can also be considered to be an unreported late phase eruptive product of the Ferra igneous group found in the western part of East Antarctica. Cretaceous plutonic rocks, similar to the granodiorite sample DG05R, are identified in Marie Byrd Land and on the Antarctic Peninsula (Leat et al., 1995; Siddoway, 2008; Vaughan et al., 2002; Veevers and Saeed, 2011 and 2013).

The provenances of the six age-determined erratics are mostly consistent with West Antarctica (Marie Byrd Land and the Antarctic Peninsula) rather than East Antarctica (Victoria Land and the Transantarctic Mountains). In particular, Triassic granitoids and upper Jurassic volcanic rocks are only reported in the Antarctic Peninsula–Thurston Island region (Figure 8b). The question of whether icebergs can migrate from the Antarctic Peninsula to the study area through the Antarctic Circumpolar Current, or whether Triassic and upper Jurassic igneous rocks, currently hidden under glaciers, are present in East Antarctica–Marie Byrd Land, should be considered by a future study.

8. Conclusions

Integrated petrological and geochemical studies of the KR1 seamount trail within the Australia–Antarctic rift system lead to the following conclusions.

(1) The KR1 seamount trail consists of alkaline OIBs and enriched tholeiites. The deep crater (DG05) is covered with various types of gravel clasts.

(2) The KR1 seamount trail is interpreted as a submarine hotspot chain based on the size and topography of the volcanic features, the occurrence of OIB with enriched tholeiites and the basalt geochemistry.

(3) The non-basaltic clasts obtained at DG05 are considered to be glacial erratics derived from Antarctica, based on their morphologies, diverse rock types, geochemical characteristics and formation ages.

(4) The main provenance of glacial erratics is considered to be the regions around the Ross Sea. Carboniferous to Cretaceous-aged glacial erratics is believed to have been from the western regions of West Antarctica.

Acknowledgments

We express our gratitude to the captain and crews of the R/V Icebreaker *Araon* for their assistance during the cruise. We also thank Dr. Youn-Joong Jeong (Korean Basic Science Institute, KBSI) for supporting the zircon U-Pb age dating and Dr. Jeongmin Kim (KBSI) for performing K-Ar age dating. Chief editor Robert J. Stern and an anonymous reviewer are appreciated for the guidance and constructive comments. We especially appreciate Philip Kyle's insightful review, which greatly improved the manuscript.

Funding

This study was supported by the Korea Polar Research Institute under Grants PE18050 and the Ministry of Ocean and Fisheries of the Republic of Korea under Grant 20140409 (PM18030).

References

Anderson, D.L., 2006, Speculation on the nature and cause of mantle heterogeneity: Tectonophysics, v. 416, p. 7-22.

Andrews, J.T., 2000, Icebergs and iceberg rafted detritus (IRD) in the North atlantics: facts and assumptions: Oceanography, v. 13, p. 100-108.

Balmer, M.D., Conrad, C.P., Smith, E.I., and Harmon, N., 2013, Non-hotspot volcano chains produced by migration of shear-driven upwelling toward the East Pacific Rise: Geology, v. 41, 479-482.

Barrett, P.J., 1975, Characteristics of pebbles from Cenozoic marine glacial sediments in the Ross Sea (DSDP sites 270-274) and the South Indian Ocean (Site 268), *in* Hayes, D.E., Frakes, L.A., Barrett, P.J., Burn, D.A., Chen, P.-H., Ford, A.B., Kaneps, A.G., Kemp, E.M., McCollum, D.W., Piper, D.J.W., Wall, R.E., and Webb, P.N., eds., Initial Reports of the Deep Sea Drilling Project, v. 28, Washington (U.S. Government Printing Office), p. 769-784.

Bischof, J., 2000, Ice drift, ocean circulation and climate change: Springer, Chichester, UK, 219 pp.

Boger, S.D., 2011, Antarctica – Before and after Gondwana: Gondwana Research, v. 19, p. 335-371.

Boger, S.D., Wilson, C.J.L., and Fanning, C.M., 2001, Early Paleozoic tectonism within the East Antarctic craton: The final suture between east and west Gondwana?: Geology, v. 29, p. 463-466.

Bourdon, B., Langmuir, C.H., and Zindler, A., 1996, Ridge-hotspot interaction along the Mid-

Atlantic Ridge between 37˚30’ and 40˚30’N: the U-Th disequilibrium evidence: Earth and Planetary Science Letter, v. 142, p. 175-189.

Burnard, P., Graham, D., and Turner, G., 1997, Vesicle-specific noble gas analyses of ‘poping rock’: Implications for primordial noble gasses in the Earth: Science, v. 276, p. 568-571.

Cande, S.C., and Stock, J.M., 2004, Pacific-Antarctic-Australia motion and the formation of the Macquarie Plate: Geophysical Journal International, v. 157, p. 399-414.

Cannat, M., Mével, C., Maia, M., Deplus, C., Durand, C., Gente, P., Agrinier, P., Belarouchi, A., Dubuisson, G., Humler, E., and Reynolds, J., 1995, Thin crust, ultramafic exposures, and rugged faulting patterns at the Mid-Atlantic Ridge (22°- 24°N): Geology, v. 23, p. 49-52.

Cawood, P.A., 2005, Terra Austalis Orogen: Rodinia breakup and development of the Pacific and Iapetus margins of Gondwana during the Neoproterozoic and Paleozoic: Earth-Science Reviews, v. 69, p. 249-279.

Choi, H., Kim, S.-S., Dyment, J., Granot, R., Park, S.-H., and Hong, J.K., 2017, The kinematic evolution of the Macquarie Plate: A case study for the fragmentation of ocean lithosphere: Earth and Planetary Science Letter, v. 478, p. 132-142.

Colling, A., 2001, Ocean circulation: Boston-Johansesburg-Melbourn-New Delhi-Oxford, The Open University, 2nd edition, 286 pp.

Collins, A.S., and Pisarevsky, S.A., 2005, Amalamating eastern Gondwana: the evolution of the Circum-India Orogens: Earth Science Review, v. 71, p. 229-270.

Collinson, J.W., Isbell, J.L., Elliot, D.H., Miller, M.F., and Miller, J.M.G., 1994, Permian-Triassic Transantarctic basin, *in* Veevers, J.J., and Powell, C.McA., eds., Permian-Triassic basins and foldbelts along the Panthalassan margin of Gondwanaland: Geological Society of America Memoir, v. 184, p. 173-222.

Dalrymple, G.B., 1969, $^{40}Ar/^{36}Ar$ analyses of historic lava flows: Earth and Planetary Science

Letter, v. 6, p. 47-55.

Dalrymple, and G.B., Moore, J.G., 1968, Argon-40: Excess in submarine pillow basalts from Kilauea volcano, Hawaii: Science, v. 161, p. 1132-1135.

Dick, H.J.B., Lin, J., and Schouten, H., 2003, An ultraslowspreading class of ocean ridge: Nature, v. 426, p. 405-412.

Dowdeswell, J.A., Maslin, M.A., Andrews, J.T., and McCave, I.N., 1995, Iceberg production, debris rafting, and the extent and thickness of Heinrich layers (H1, H-2) in North Atlantic sediments: Geology, v. 23, 301-304.

Eggler, D.H., 1974, Effect of CO_2 on the melting of peridotite: Carnegie Institution of Washington Yearbook, v. 74, p. 215-224.

Elliot. D.H., 2013, The geological and tectonic evolution of the Transantarctic Mountains: a review, *in* Hambrey, M.J., Baker, P.F., Barrett, P.J., Bowman, V., Davies, B., Smellie, J.L., and Tranter, M., eds., Antarctic palaeoenvironments and Earth-surface processes: Geological Society of London Special Publication, no. 381, http://dx.doi.org/10.1144/SP381.14.

Finn, C.A., Muller, R.D., and Panter, K.S., 2005, A Cenozoic diffuse alkaline magmatic province (DAMP) in the southwest Pacific without rift or plume origin: Geochemistry, Geophysics, Geosystems, v. 6, doi:10.1029/2004GC000723.

Fisher, 1981, Quantitative retention of magmatic argon in a glassy basalt: Nature, v. 290, p. 42-43.

Fitton, J.G., Saunders, A.D., Norry, M.J., Hardarson, B.S., and Taylor, R.N., 1997, Thermal and chemical structure of the Iceland plume: Earth and Planetary Science Letters, v. 153, p. 197-208.

Fitton, J.G., 2007, The OIB paradox, *in* Foulger, G.R. and Jurdy, D.M., eds., Plates, plumes and planetary processes: Geological Society of America Special Paper 430, Boulder, Colorado, doi: 10.1130/2007.2430(20).

Fitzsimons, I.C.W., 2000, A review of tectonic events in the East Antarctic Shield and their implications for Gondwana and earlier supercontinents: Journal of African Earth Sciences, v. 31, p. 3-23.

Frey, F.A., Huang, S., Blichert-Tort, J., Regelous, M., and Boyet, M., 2005, Origin of depleted components in basalt related to the Hawaiian hot spot: Evidence from isotopic and incompatible element ratios: Geochemistry, Geophysics, Geosystems, v. 6, Q02L07, doi:10.1029/2004GC000757.

Garcia, M.O., Foss, D.J.P., West, H.B., and Mahoney, J.J., 1995, Geochemical and isotopic evolution of Loihi volcano, Hawaii: Journal of Petrology, v. 36, p. 1647-1674.

Gilbert, R., 1990, Rafting in glacimarine environments, *in* Dowdeswell, J.A., and Scourse, J.D., eds., Glacimarine environments: Processes and sediments: Geological Society Special Publication, no. 53, p. 105-120.

Graham, D.W., 2002, Noble gas isotope geochemistry of mid-ocean ridge and ocean island basalts: Characterization of mantle source reservoirs, *in* Porcelli, D., Ballentine, C.J., and Wieler, R., eds., Noble gases in geochemistry and cosmochemistry: Reviews in Mineralogy and Geochemistry, Mineralogical Society of America, Washington DC, p. 247-318.

Hahm, D., Baker, E.T., Rhee, T.S., Won, Y.-J., Resing, J.A., Lupton, J.E., Lee, W.-K., Kim, M., and Park, S.-H., 2015, First hydrothermal discoveries on the Australian-Antarctic Ridge: Discharge sites, plume chemistry, and vent organisms: Geochemistry Geophysics Geosystems, v. 16, p. 3061-3075, doi:10.1002/2015GC005926.

Hanan, B.B., and Schilling, J.-G., 1997, The dynamic evolution of the Iceland mantle plume: the lead isotope perspective: Earth and Planetary Science Letters, v. 151, p. 43-60.

Hanan, B.B., Blichert-Toft, J., Pyle, D.G., and Christie, D.M., 2004, Cantrasting origins of the upper mantle revealed by hafnium and lead isotopes form the Southeast Indian Ridge:

Nature, v. 432, p. 91-94.

Harley, S.L., and Kelly, N.M., 2007, Ancient Antarctica; the Archean of the East Antarctic, *in* Van Kranendonk, M.J., Smithies, R.H., and Bennett, V.C., eds, Earth's oldest rocks: Developments in Precambrian Geology, v. 15, pp. 149-186.

Hart, S.R., and Kyle, P.R., 1993, Geochemistry of McMurdo Group volcanic rocks: Antarctic Journal U.S., v. 28, p.14-16.

Hirano, N., Takahashi, E., Yamamoto, J., Abe, N., Ingle, S.P., Kaneoka, I., Hirata, T., Kimura, J.-I., Ishii, T., Ogawa, Y., Machido, S., and Suyehiro, K., 2006, Volcanism in response to plate flexure: Science, v. 313, p. 1426-1428.

Ildefonse, B., Blackman, D.K., John, B.E., Ohara, Y., Miller, D.J., MacLeod, C.J., and Expedition Scientific Party, 2007, Ocean core complexes and crustal accretion at slow-spreading ridge: Geology, v. 35, p. 623-626.

Ivrine, T.N., and Baragar, W.R.A., 1971, A guide to the chemical classification of the common volcanic rocks: Canadian Journal of Earth Sciences, v. 8, p. 523-548.

Jacobs, J., 2009, A review of two decade (1986-2006) of geochronological work in Heimfrontfjella and geotectonic interpretation of western Dronning Maud Land, East Antractica: Polarforschung, v. 79, p. 47-57.

Janney, P.E., Macdougall, J.D., Natland, J.H., and Lynch, M.A., Geochemical evidence from the Pukapuka volcanic ridge system for a shallow enriched mantle domain beneath the South Pacific Superswell: Earth and Planetary Science Letters, v. 181, p. 47-60.

Kempton, P.D., Pearce, J.A., Barry, T.L., Fitton, J.G., Langmuir, C., and Christie, D.M., 2002, Sr-Nd-Pb-Hf isotope results from ODP Leg 187: Evidence for mantle dynamics of the Autralian-Antarctic Discordance and origin of the Indian MORB source: Geochemistry Geophysics Geosystems, v. 3, 1074, doi:10.1029/2002GC000320.

Koppers, A.A.P., 2011, Mantle plumes persevere: Nature Geoscience, v. 4, p. 816-817.

Kim, J., 2001, New K-Ar system in Korea Basic Science Institute: Summary and performance: The Journal of the Petrological Society of Korea, v. 10. p. 172-178.

Kinzler, R.J., and Grove, T.L., 1993, Corrections and further discussion of the primary magmas of mid-ocean ridge basalts, 1 and 2: Journal of Geophysical Research, v. 98, p. 22339-22347.

Kuno, H., 1966, Lateral variation of basalt magma types across continental margins and island arcs: Bulletin of Volcanology, v. 29, p. 195-222.

Kushiro, I., 1996, Partial melting of a fertile mantle peridotite at high pressures: An experimental study using aggregates of diamond, *in* Basu, A. and Hart, S.R., eds., Earth processes: Reading the isotopic code: Geophygical Monograph 95, American Geophysical Union, Washington, DC, p. 109-122.

Kushiro, I., 2001, Partial melting experiments on peridotite and origin of mid-ocean ridge basalt: Annual Review of Earth and Planetary Science, v. 29, p. 71-107.

Lanyon, R., Varne, R., and Crawford, A.J., 1993, Tasmanian Tertiary basalts, the Balleny plum, and opening of the Tasman Sea (southwest Pacific Ocean): Geology, v. 21, p. 555-558.

Leat, P.T., Scarrow, J.H.,and Millar, I.L., 1995, On the Antarctic Peninsula batholith: Geological Magazine, v. 132, p. 399-412.

Le Bas, M.J., Maitre, R.W., Streckeisen, A., and Zanettin, B., 1986, A chemical classification of volcanic rocks based on the total alkali-silica diagram: Journal of Petrology, v. 27, p. 745-750.

Licht, K.J., and Hemming, S.R., 2017, Analysis of Antarctic glacigenic sediment provenance through geochemical and petrologic applications: Quaternary Science Review, v. 164, p. 1-24.

Ludwig, K.R., 2003, User's manual for Isoplot/Ex version 3.00: A Geochronological Toolkit for Mircosoft Excel: Berkeley Geochronology Center Special publication, no. 4, Berkeley, California. 70 p.

McDonald, G.A., 1968, Composition and origin of Hawaiian lavas, *in* Coats, R.R., Hay, R.L., and Anderson, C.A. ,eds., Studies in volcanology: a memoir in honour of Howel Williams: Geological Society of American Memoirs, no. 116, p. 477-522.

Mcdonald, G.A., and Kstsura, T., 1964, Chemical composition of Hawaiian lavas: Journal of Petrology, v. 5, p. 83-133.

McKenzie, D., and O'Nions, R.K., 1991, Partial melt distributions from inversion of rare-earth element concentrations: Journal of Petrology, v. 32, p. 1021-1091.

McNutt, K.K., 2006, Another nail in the plume coffin?: Science, v. 313, p. 1394-1395.

Meschede, M., 1986, A method of discriminating between different types of mid-ocean ridge basalts and continental tholeiites with the Nb-Zr-Y diagram: Chemical Geology. V. 56, p. 558-569.

Middlemost, E.A.K., 1994, Naming materials in the magma/igneous rock system: Earth Science Reviews, v. 37, p. 215-224.

Morgan, W.J., 1971, Convection plumes in the lower mantle: Nature, v. 230, p. 42-43.

Mori, Y., Mashima, H., 2005, X-ray fluorescence analysis of major and trace elements in silicate rocks using 1:5 dilution glass beads: Bulletin of the Kitakyushu Museum of Natural History and Human History Series A, v. 3, p. 1-12.

Moriera, M., Kunz, J., and Allègre, C., 1998, Rare gas systematics in poping rock: Isotopic and elemental compositions in the upper mantle: Science, v. 279, p. 1178-1181.

Nagao, K, Ogata, A., Miura, Y.N., and Yamaguchi, K., 1996, Ar isotope analysis for K-Ar dating using two modified-VG5400 mass spectrometers-I: Isotope dilution method: Journal of the Mass Spectrometry Society of Japan, v. 44, p. 39-61.

Niu, Y., and Batiza, R., 1997, Trace element evidence from seamounts for recycled oceanic crust in the Eastern Pacific mantle: Earth and Planetary Science Letters, v. 148, p. 471-483.

Niu, Y., Regelous, M., Wendt, I.J., Batiza, R., and O'Hara, M.J., 2002, Geochemistry of near-

EPR seamounts: importance of source vs. process and the origin of enriched mantle component: Earth and Planetary Science Letters, v. 199, p. 327-345.

Ozima, M., Saito, K., and Honda, M., 1977, Sea water weathering effect on K-Ar age of submarine basalts: Geochimica et Cosmochimica Acta., v. 41, p. 453-461.

Pankhurst, R.J., Weaver, S.D., Bradshaw, J.D., Storey, B.C., and Ireland, T.R., 1998, Geochronology and geochemistry of pre-Jurassic superterranes in Marie Byrd Land, Antarctica: Journal of Geophysical Research, v. 103, p. 2529-2547.

Pankhurst, R.J., Riley, T.R., Fanning, C.M., and Kelley, S.P., 2000, Episodic silicic volcanism in Patagonia and the Antarctic Peninsula: chronology of magmatism associated with the break-up of Gondwana: Journal of Petrology, v. 41, p. 605-625.

Paton, C., Hellstrom, J., Paul, B., Woodhead, J., and Hergt, J., 2011, Iolite: Freeware for the visualization and procession of mass spectrometric data: Jouranl of Analytical Atomic Spectrometry, v. 26, p. 2508-2518.

Pearce, J.A., 1996, Sources and settings of granitic rocks: Episodes, v. 19, p. 120-125.

Peccerillo, A., and Taylor, S.R., 1976, Geochemistry of Eocene calc-alkaline volcanic rocks in the Kastamonu area, Northern Turkey: Contributions to Mineralogy and Petrology, v. 58, p. 63-81.

Phipps Morgan, J., 1999, Isotope topology of individual hotspot basalts arrays: Mixing curves or melt extraction trajectories?: Geochemistry, Geophysics, Geosystems, v. 1, 1999GC000004.

Phipps Morgan, J., and Morgan, W.J., 1999, Two-stage melting and the geochemical evolution of the mantle: A recipe for mantle plum-pudding: Earth and Planetary Science Letters, v. 170, p. 215-239.

Regelous, A.H.F., Hofmann, A.W., Abouchami, W., and Galer, S.J.G., 2003, Geochemistry of lavas from the Emperor Seamounts, and the geochemical evolution of Hawaiian magmatism

from 85 to 42 Ma: Journal of Petrology, v. 44, p. 113-140.
Rignot, E., Bamber, J.L., van den Broeke, M.R., Davis, C., Li, Y., van de Berg, W.J., and van Meijgaard, E., 2008, Recent Antarctic ice mass loss from radar interferometry and regional climate modelling: Nature Geoscience, v. 1, p. 106-110.
Rocchi, S., Armienti, P., D'Orazio, M., Tonarini, S., Wijbrans, J.R., and Di Vincenzo, G., 2002, Cenozoic magmatism in the western Ross Embasyment: Role of mantle plume versus plate dynamics in the development of the West Antarctic Rift System: Journal of Geophysical Research, v. 107, doi: 10.1029/2001JB000515.
Rocchi, S., Bracciali, L., Di Vincenzo, G., Gemelli, M., Ghezzo, C., 2011, Arc accretion to the early Paleozoic Antarctic margin of Gondwana in Victoria Land: Gondwana Research, v. 19, p. 594-607.
Salters, V.J.M., and Longhi, J., 1999, Trace element partitioning during the initial stages of melting beneath mid-ocean ridges: Earth and Planetary Science Letters, v. 166, p. 15-30.
Sauter, D., and Cannat, M., 2010, The ultraslow spreading Southwest Indian Ridge: Diversity of hydrothermal systems on slow spreading ocean ridges: Geophysical Monograph Series, no. 188, Washington DC, The American Geophysical Union, p. 153-173.
Seidemann, D.E., 1977, Effects of submarine alteration on K-Ar dating of deep-sea igneous rocks: Geological Society of America Bulletin, v. 88, p. 1660-1666.
Siddoway, C.S., 2008, Tectonics of the West Antarctic Rift System: new light on the history and dynamics of distributed intracontinental extension, *in* Cooper, A.K., Barrett, P.J., Stagg, H., Storey, B., Stump, E., Wise, W., and the 10th ISAES editorial team, eds., Antarctica: A keyston in a changing world: Proceedings of the 10th International Symposium on Antarctic Earth Sciences, The National Academies Press, Washington, DC, pp. 91-114.
Siddoway, C.S., and Fanning, C.M., 2009, Paleozoic tectonism on the East Gondwana margin: Evidence from SHRIMP U-Pb zircon geochronology of a migmatite-granite complex in

West Antarctica: Tectonophysics, v. 477, p. 262-277.

Slama, J., Kosler, J., Condon, D.J., Crowley, J.L., Gerdes, A., Hanchar, J.M., Horstwood, M.S.A., Morris, G.A., Nasdala, L., Norberg, N., Schaltegger, U., Schoene, B., Tubrett, M.N., and Whitehouse, M.J., 2008, Plesovice zircon - a new natural reference material for U-Pb and Hf isotopic microanalysis: Chemical Geology, v. 249, p. 1-35.

Staudigel, H., and Clague, D.A., 2010, The geological history of deep-sea volcanoes: Biosphere, hydrosphere, and lithosphere interactions: Oceanography, v. 23, p. 56-71.

Storey, B.C., Vaughan, A.P.M., and Millar, I.L., 1996, Geodynamic evolution of the Antarctic Peninsula during Mesozoic times and its bearing Weddell Sea history: Geological Society of London Special Publications, v. 108, p. 87-103.

Storey, B.C., Vaughan, A.P.M., and Riley, T.R., 2013, The links between large igneous provinces, continental break-up and environmental chage: evidence reviewed from Antarctica: Earth and Environmental Science Transactions of the Royal Society of Edinburgh, v. 104, 17-30.

Sun, S.S., and McDonough, W.F., 1989, Chemical and isotopic systematic of oceanic basalt: implications for mantle composition and processes, *in* Saunders, A.D., and Norry, M.J., eds., Magmatism in the ocean basins: Geological Society Special Publication, no. 42, The Geological Society of London, London, p. 313-345.

Tucholke, B.E., Behn, M.D., Buck, W.R., and Lin, J., 2008, Role of melt supply in oceanic detachment faulting and formation of megamullions: Geology, v. 36, p. 455-458.

Vaughan, A.P.M., Pankhurst, R.J., and Fanning, C.M., 2002, A mid-Cretaceous age for the Palmer Land event, Antarctic Peninsula: implications for terrane accretion and Gondwana palaeolatitudes: Journal of the Geological Society of London, v. 159, p. 113-116.

Vaughan, D.G., Comiso, J.C., Allison, I., Carrasco, J., Kaser, G., Kwok, R., Mote, P., Murray, T., Paul, F., Ren, J., Rignot, E., Solomina, O., Steffen, K., and Zhang, T., 2013, Observations:

Crysophere, *in* Stocker, T.F., Qin, D., Platter, G.-K., Tignor, M., Allen, S.K., Boschung, J., Nauels, A., Xia, Y., Bex, V., and Midgley, P.M., eds., Climate change 2013. The physical science basis: Contribution of working group I to the fifth assessment report of the intergovernmental panel on climate chage: Cambridge University Press, Cambridge, United Kingdom and New York, NY, USA.

Veevers, J.J., and Saeed, A., 2011, Age and composition of Antarctic bedrock reflected by detrital zircons, erratics, and recycled microfossils in the Prydz Bay-Wilkes Land-Ross Sea-Marie Byrd Land sector (70˚-240˚E): Gondwana Research, v. 20, p. 710-738.

Veevers, J.J., and Saeed, A., 2013, Age and composition of Antarctic sub-glacial bedrock reflected by detrital zircons, erratics, and recycled microfossils in the Ellsworth Land-Antrarctic Peninsula-Weddell Sea-Dronning Maud Land sector (240˚-0˚-015˚E): Gondwana Research, v. 23, p. 296-332.

Vlastelic, I., and Dosso, L., 2005, Initiation of a plune-ridge interaction in the South Pacific recorded by high-precision Pb isotopes along Hollister Ridge: Geochemistry, Geophysics, Geosystems, v. 6, Q05011, doi: 10.1029/2004GC000902.

Wessel, P., Sandwell, D.T., and Kim, S.-S., 2010, The global seamount census: Oceanography, v. 23, p. 24-33.

White, W.M., and Duncan, R.A., 1993, Petrology and geochemistry of the Galapagos Islands – portrait of a pathological mantle plume: Journal of Geophysical Research, v. 102, p. 22459-22475.

Wiedenbeck, M., Alle, P., Corfu, F., Griffin, W.L., Merier, M., and Ober, F., 1995, Three natural zircon standards for U-Th-Pb, Lu-Hf, trace element and REE analyses: Geostandards Newsletter, v. 19, p. 1-23.

Winchester, J.A., and Floyd, P.A., 1976, Geochemical magma type discrimination; application to altered and metamorphosed basic igneous rocks: Earth and Planetary Science Letters, v. 28, p. 459-469.

Yamamoto, M., Phipps Morgan, J., and Morgan, W.J., 2007, Global plume-fed asthenosphere flow-II: Application to the geochemical segmentation of mid-ocean ridges, *in* Foulger, G.R. and Jurdy, D.M., eds., Plates, plumes and planetary processes: Geological Society of America Special Paper v. 430, p. 165-188, Geological Society of America, Boulder, Colorado. doi: 10.1130/2007.2430(10)

Yi, S.-B., Oh, C.W., Pak, S.J., Kim, J., and Moon, J.-W., 2014, Geochemistry and petrogenesis of mafic-ultramafic rocks from the Central Indian Ridge, latitude 8˚-17˚S: denudation of mantle harzburgites and gabbroic rocks and compositional variation of basalts: International Geology Review, v. 56, p. 1691-1719.

Figure captions

Figure 1. (a) Regional map of the Southern Ocean showing the Australian-Antarctic Ridge (AAR) and the KR1 segment. Previous research regions around the KR1 segment and their references: 1, Choi et al. (2017); 2, Hahm et al. (2015); 3, Lanyon et al., 1993; 4, Hanan et al. (2004); 5, Kempton et al. (2002); 6, Cande and Stock (2004). The satellite image is taken from Google Earth. (b) Bathymetric map of the KR1 study area (modified from Hahm et al., 2015) with ocean floor ages estimated from magnetic anomaly (after Choi et al., 2017). Arrows on the map indicate seamounts with the height of more than 1000 m. (c) Enlarged map showing the study area (KR1 seamount trail) and sampling locations with dredged rock types and their K-Ar ages. Various rock clasts in the DG05 include mafic plutonic rocks, granitoids and various volcanic and sedimentary rocks. Abbreviations: SEIR, Southeast Indian Ridge; PAR, Pacific-Antarctic Ridge; Jct., Junction; ol basalt, olivine basalt (alkali basalt); thol., tholeiite.

Figure 2. Photomicrographs and backscattered electron (BSE) images of basaltic rocks: (a) normal basalt (DG05-1C) with glass crust, (b) BSE image of the glass part of the DG05-1C, (c) olivine basalt (DG05A), (d) glassy olivine basalt (DG04-2), (e) glassy olivine basalt (DG04-1) and (f) BSE image of the DG04-1. The photos of (a, d and e) were taken under plane-polarized light, and the photo of (c) was taken under cross-polarized light. Abbreviations: pl, plagioclase; cpx, clinopyroxene; ol, olivine; Mn, manganese compound; Cr-spl, chromian spinel.

Figure 3. Geochemical classification of basalts and other rock clasts on the (a) total alkali *versus* silica (TAS) diagram (after Le Bas et al., 1986) with the subdivision into alkaline, subalkaline and transitional (after McDonald and Katsura ,1964; Kuno, 1966; McDonald, 1968; Irvine and Baragar, 1971), (b) the K_2O *versus* SiO_2 diagram (after Peccerillo and Taylor, 1976), (c) the Nd/Y *versus* $Zr/(P_2O_5 \times 10^4)$ discrimination diagram (Winchester and Floyd, 1976), (d) the Nb-Zr-Y discrimination diagram (after Meschede, 1986) and (e) the Rb *versus* Y+Nb discrimination diagram (after Pearce, 1996). The plutonic rock names in the TAS diagram (a) follow the names in the Middlemost (1994). Major element concentrations (a, b) were recalculated to 100 percent on a volatile-free basis. Abbreviations: MORB, mid-ocean ridge basalt; E, enriched; N, normal; Syn-COLG, syn-collisional granites; VAG, volcanic arc granites; WPG, within plate granites; ORG, oceanic ridge granites.

Figure 4. Chondrite-normalized rare earth element (REE) and N-MORB-normalized multi-element variation diagrams of the alkaline basalts and the tholeiites. The normalization values and MORB and ocean island basalt (OIB) compositions are taken from Sun and McDonough (1989).

Figure 5. Chondrite-normalized REE and N-MORB-normalized multi-element variation diagrams of various rock clasts such as gabbroic diorite, granitoids and volcanic rocks from

the DG05 depression. The normalization values are taken from Sun and McDonough (1989).

Figure 6. Zircon U-Pb age dating results of plutonic rock clasts from the DG05 depression: concordia diagrams with weighted mean $^{206}Pb/^{238}U$ ages for (a) the gabbroic diorite (DG05W), (b) the granodiorite (DG05R) and (c, d) granites (DG05H and DG05I).

Figure 7. Chondrite-normalized Tb/Yb_N *versus* Lu/Hf_N values for alkali basalts and tholeiites (after Janney et al., 2000). Grids exhibit melts compositions produced by 1, 5 and 10 % of incremental batch melting with the presence of residual garnet (0-100 %) and spinel (100-0%). The modes and melting proportions of olivine, orthopyroxene, clinopyroxene and spinel-garnet for the modelling are 0.43/0.3/0.1/0.07 and 0.1/0.1/0.4/0.4, respectively. Partition coefficients for pyroxene and garnet are taken from Salters and Longhi (1999), and those for olivine and spinel are taken from McKenzie and O'Nions (1991).

Figure 8. (a) Glacier outflow indicated in order of size (e.g., #1 = 237 Gt/yr; #19 = 9 Gt/yr; Rignot et al., 2008), mean circulation patterns of sea ice (Vaughan et al, 2013) and ocean surface currents (light blue arrows) around Antarctica with the Antarctic Circumpolar Current (dark blue arrows; Colling, 2001). The ice drainage basin (Rignot et al., 2008), which can supply major icebergs in the study area, is highlighted in yellow. (b) Geological map of Antarctica with the outcrop location related to the age-determined glacial erratics of the DG05 depression (modified from Collins and Pisarevsky, 2005; Elliot, 2013; Licht and Hemming, 2017).

Supplementary Figure captions

Supplementary Figure 1. Dredged basaltic rock samples from (a, b) the DG05, (c) DG04 and (d) DG03 areas.

Supplementary Figure 2. Various types of rock clasts from the DG05 area: (a) mafic plutonic rocks, (b) various granitoids, (c) various volcanics and (d) sedimentary rocks including deformed greywacke and sandstone.

Supplementary Table captions

Supplementary Table 1. Representative whole-rock major and trace element compositions of basalts and non-basaltic clasts.

Supplementary Table 2. K-Ar age determination data of basalts and other volcanic rock clasts.

Supplementary Table 3. Zircon U-Pb age dating results of plutonic rock clasts in the DG05 dredge.

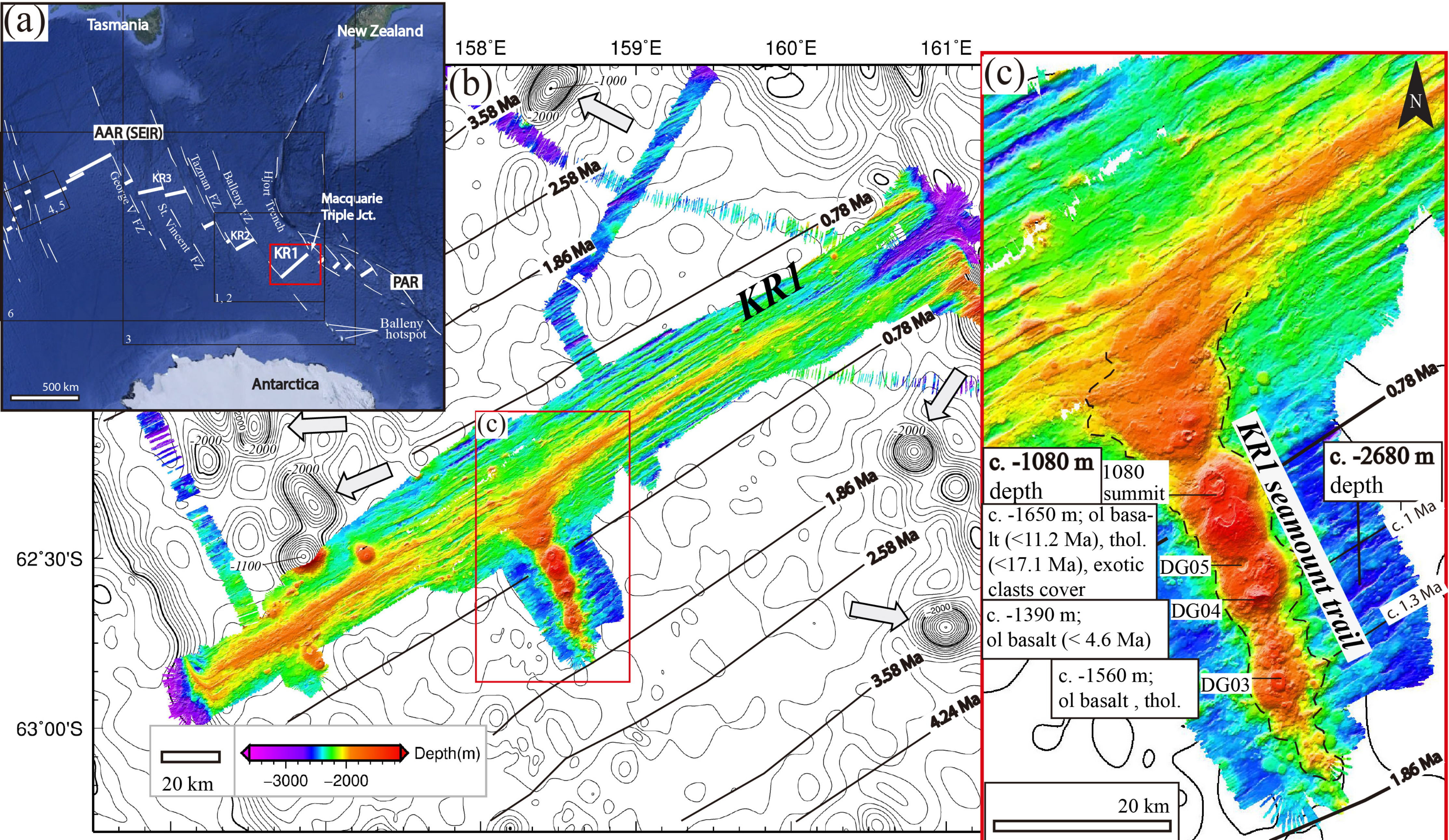
(a)
Tasmania
New Zealand
AAR (SEIR)
KR3
KR2
KR1
George V FZ
St. Vincent FZ
Tazman FZ
Balleny FZ
Hjort Trench
Macquarie Triple Jct.
PAR
Balleny hotspot
Antarctica
500 km
(b)
158˚E
159˚E
160˚E
161˚E
156˚E
157˚E
62˚30'S
63˚00'S
3.58 Ma
2.58 Ma
1.86 Ma
0.78 Ma
4.24 Ma
KR1
-1000
-2000
-1100
20 km
Depth(m)
−3000
−2000
(c)
N
c. -1080 m depth
1080 summit
c. -2680 m depth
c. -1650 m; ol basalt (<11.2 Ma), thol. (<17.1 Ma), exotic clasts cover
c. -1390 m; ol basalt (< 4.6 Ma)
c. -1560 m; ol basalt , thol.
DG05
DG04
DG03
KR1 seamount trail
c. 1 Ma
c. 1.3 Ma
0.78 Ma
1.86 Ma
20 km
Figure 1

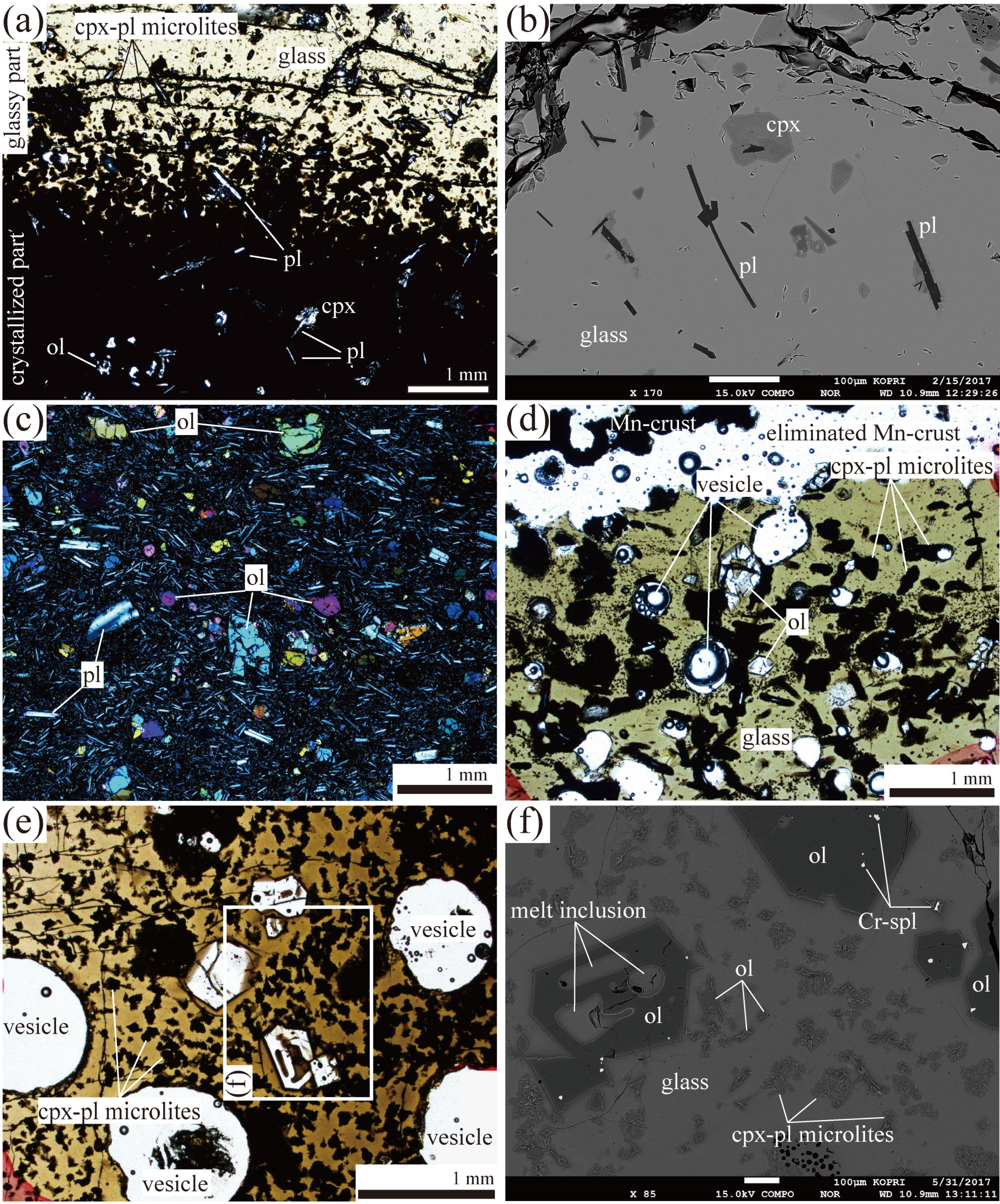
(a)
cpx-pl microlites
glass
glassy part
crystallized part
pl
cpx
ol
pl
1 mm
(b)
cpx
pl
pl
glass
100μm KOPRI 2/15/2017
X 170 15.0kV COMPO NOR WD 10.9mm 12:29:26
(c)
ol
ol
pl
1 mm
(d)
Mn-crust
eliminated Mn-crust
cpx-pl microlites
vesicle
ol
glass
1 mm
(e)
vesicle
vesicle
(f)
cpx-pl microlites
vesicle
vesicle
1 mm
(f)
ol
Cr-spl
melt inclusion
ol
ol
ol
glass
cpx-pl microlites
100μm KOPRI 5/31/2017
X 85 15.0kV COMPO NOR WD 10.9mm 13:11:11

Figure 2

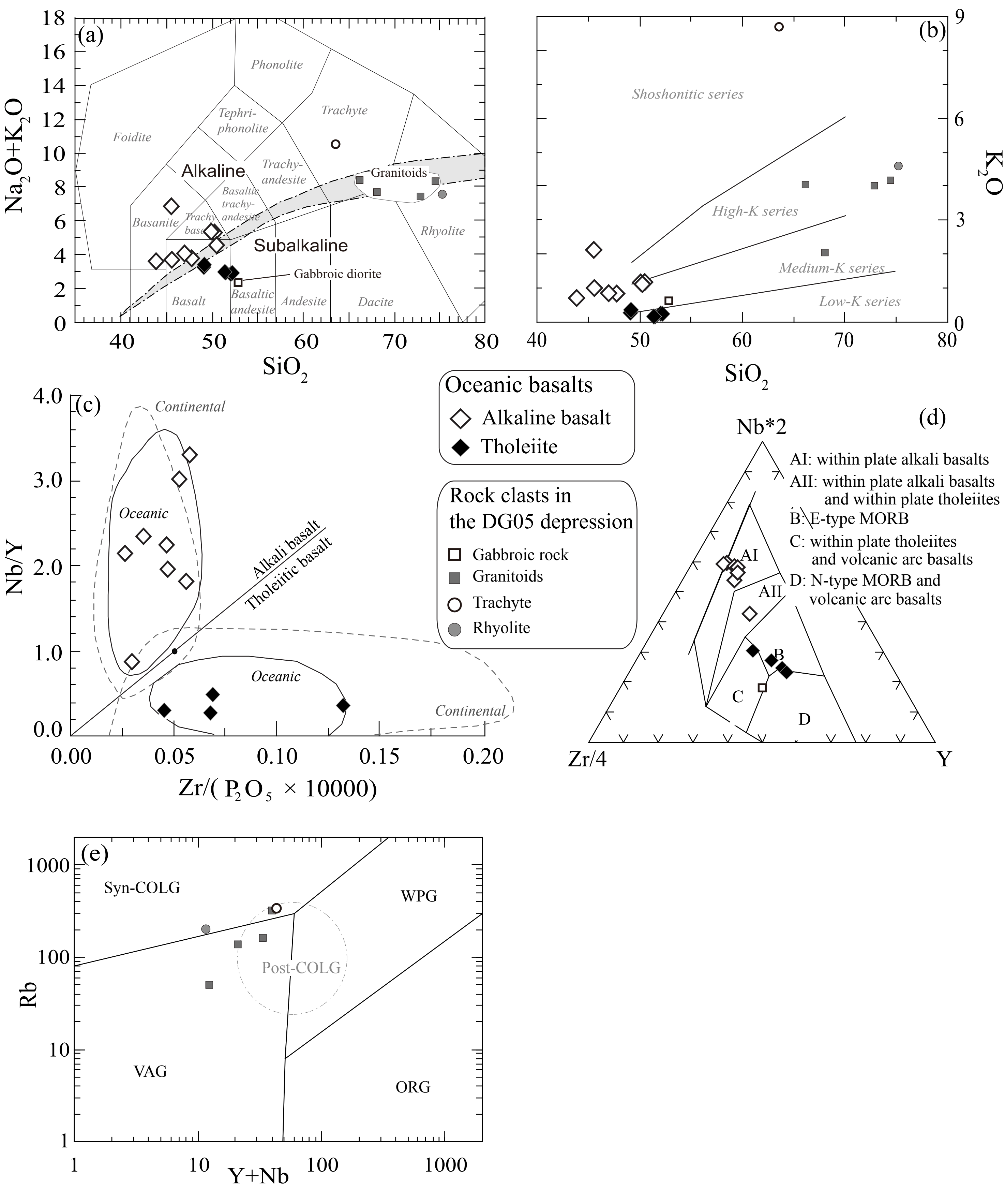
(a)
Na2O+K2O
SiO2
Foidite
Phonolite
Tephri-phonolite
Trachyte
Alkaline
Trachy-andesite
Granitoids
Basanite
Basaltic trachy-andesite
Subalkaline
Rhyolite
Gabbroic diorite
Basalt
Basaltic andesite
Andesite
Dacite
(b)
K2O
Shoshonitic series
High-K series
Medium-K series
Low-K series
(c)
Nb/Y
Zr/(P2O5 × 10000)
Continental
Oceanic
Alkali basalt
Tholeiitic basalt
Oceanic basalts
Alkaline basalt
Tholeiite
Rock clasts in the DG05 depression
Gabbroic rock
Granitoids
Trachyte
Rhyolite
(d)
Nb*2
Zr/4
Y
AI: within plate alkali basalts
AII: within plate alkali basalts and within plate tholeiites
B: E-type MORB
C: within plate tholeiites and volcanic arc basalts
D: N-type MORB and volcanic arc basalts
AI
AII
B
C
D
(e)
Rb
Y+Nb
Syn-COLG
WPG
Post-COLG
VAG
ORG

Figure 3

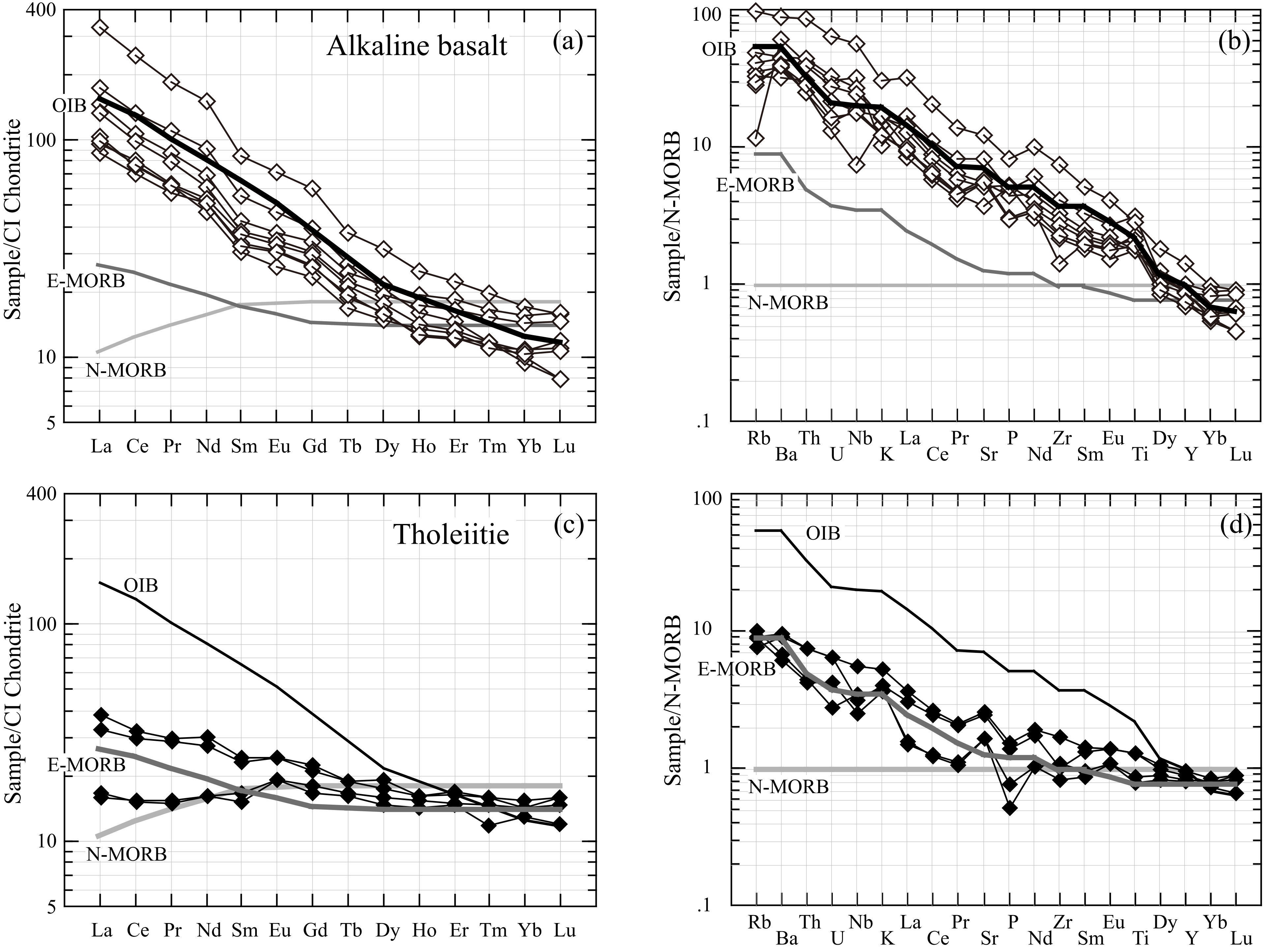

Alkaline basalt
(a)
OIB
E-MORB
N-MORB
Sample/CI Chondrite
400
100
10
5
La Ce Pr Nd Sm Eu Gd Tb Dy Ho Er Tm Yb Lu
(b)
OIB
E-MORB
N-MORB
Sample/N-MORB
100
10
1
.1
Rb Ba Th U Nb K La Ce Pr Sr P Nd Zr Sm Eu Ti Dy Y Yb Lu
Tholeiitie
(c)
OIB
E-MORB
N-MORB
Sample/CI Chondrite
400
100
10
5
La Ce Pr Nd Sm Eu Gd Tb Dy Ho Er Tm Yb Lu
(d)
OIB
E-MORB
N-MORB
Sample/N-MORB
100
10
1
.1
Rb Ba Th U Nb K La Ce Pr Sr P Nd Zr Sm Eu Ti Dy Y Yb Lu

Figure 4

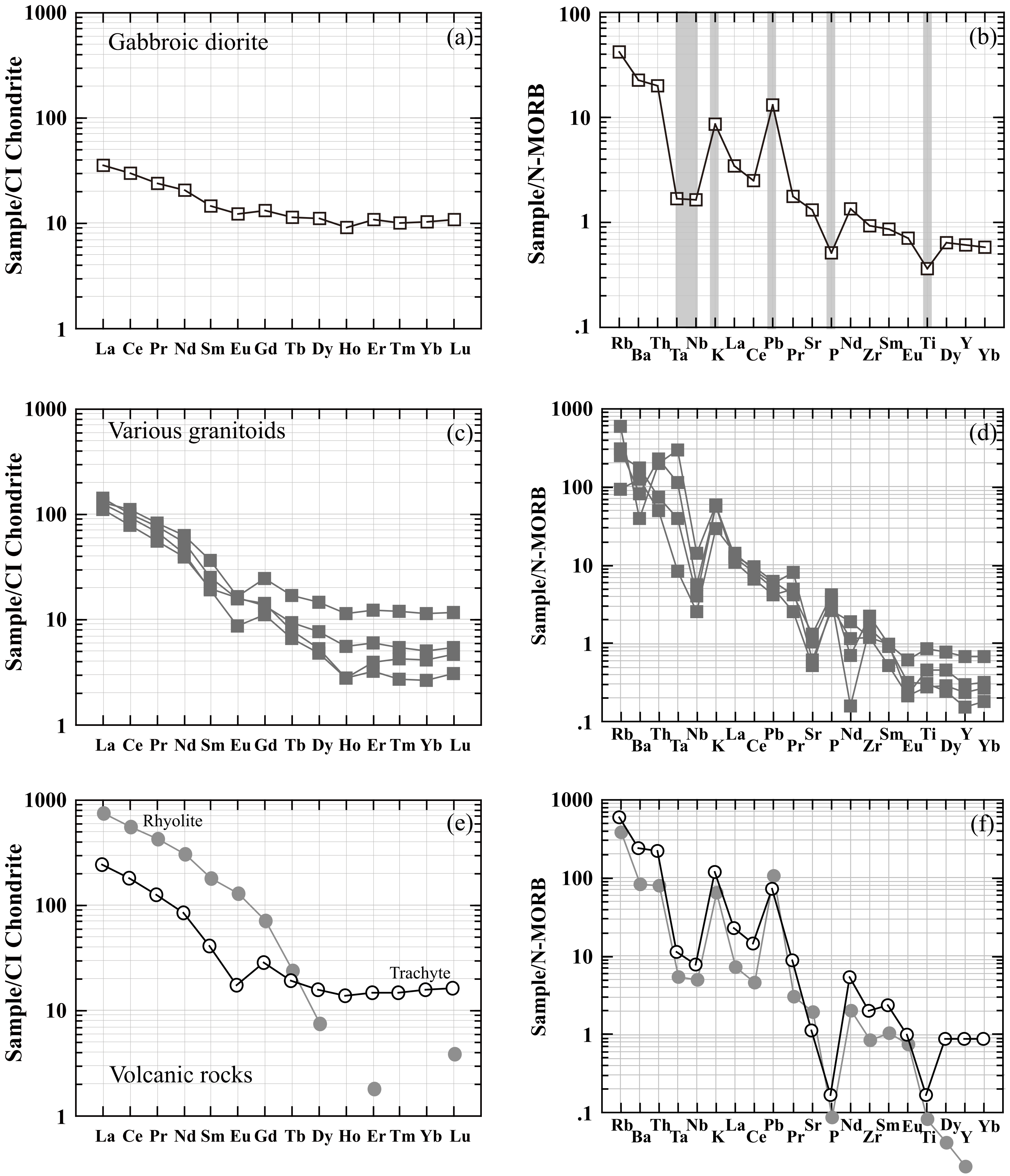

Gabbroic diorite
(a)
Sample/CI Chondrite
1000
100
10
1
La Ce Pr Nd Sm Eu Gd Tb Dy Ho Er Tm Yb Lu
(b)
Sample/N-MORB
100
10
1
.1
Rb Ba Th Ta Nb K La Ce Pb Pr Sr P Nd Zr Sm Eu Ti Dy Y Yb
Various granitoids
(c)
(d)
1000
Rhyolite
Trachyte
Volcanic rocks
(e)
(f)

Figure 5

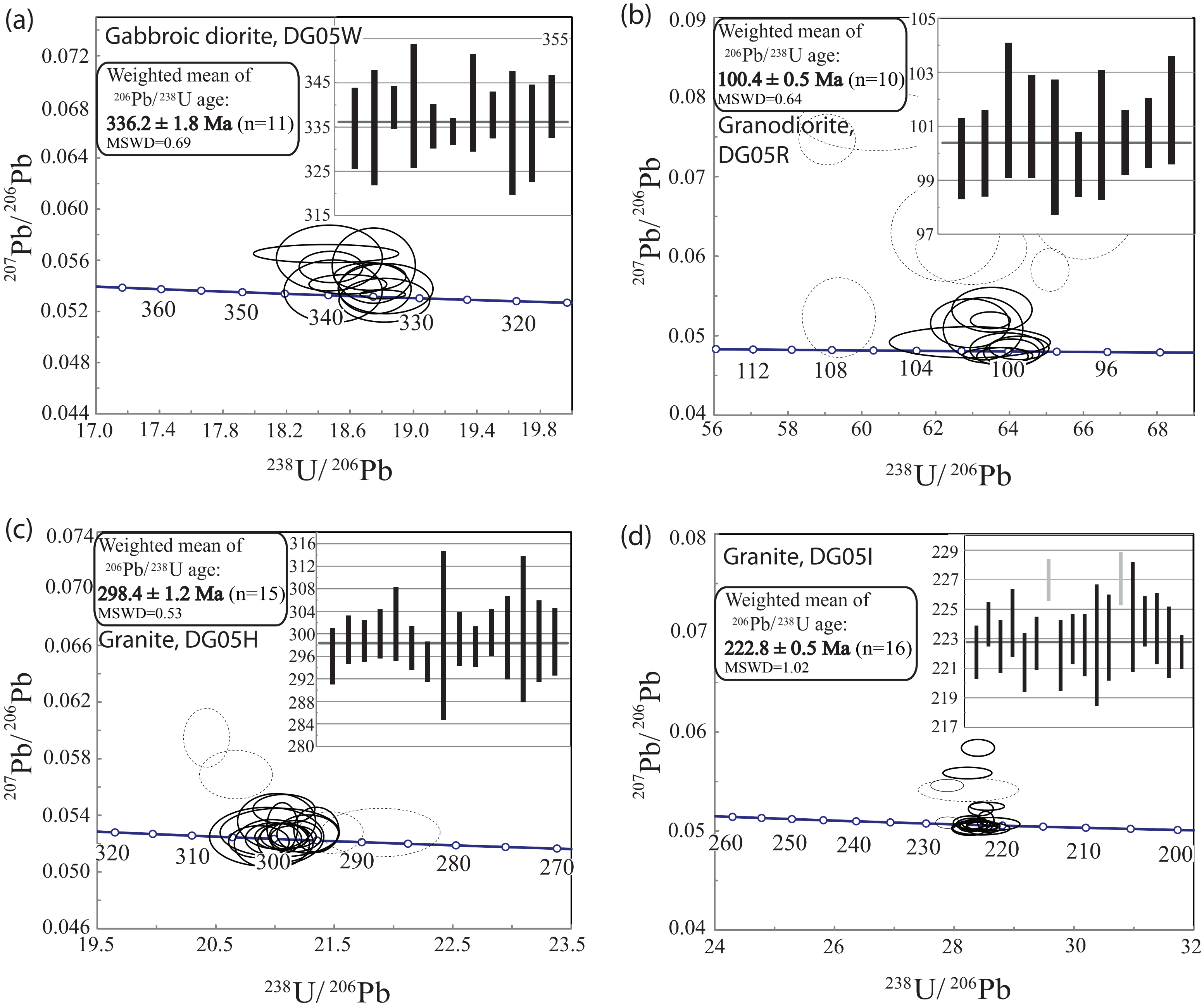

(a)
Gabbroic diorite, DG05W
Weighted mean of $^{206}Pb/^{238}U$ age:
336.2 ± 1.8 Ma (n=11)
MSWD=0.69
$^{207}Pb/^{206}Pb$
$^{238}U/^{206}Pb$
(b)
Weighted mean of $^{206}Pb/^{238}U$ age:
100.4 ± 0.5 Ma (n=10)
MSWD=0.64
Granodiorite, DG05R
$^{207}Pb/^{206}Pb$
$^{238}U/^{206}Pb$
(c)
Weighted mean of $^{206}Pb/^{238}U$ age:
298.4 ± 1.2 Ma (n=15)
MSWD=0.53
Granite, DG05H
$^{207}Pb/^{206}Pb$
$^{238}U/^{206}Pb$
(d)
Granite, DG05I
Weighted mean of $^{206}Pb/^{238}U$ age:
222.8 ± 0.5 Ma (n=16)
MSWD=1.02
$^{207}Pb/^{206}Pb$
$^{238}U/^{206}Pb$

Figure 6

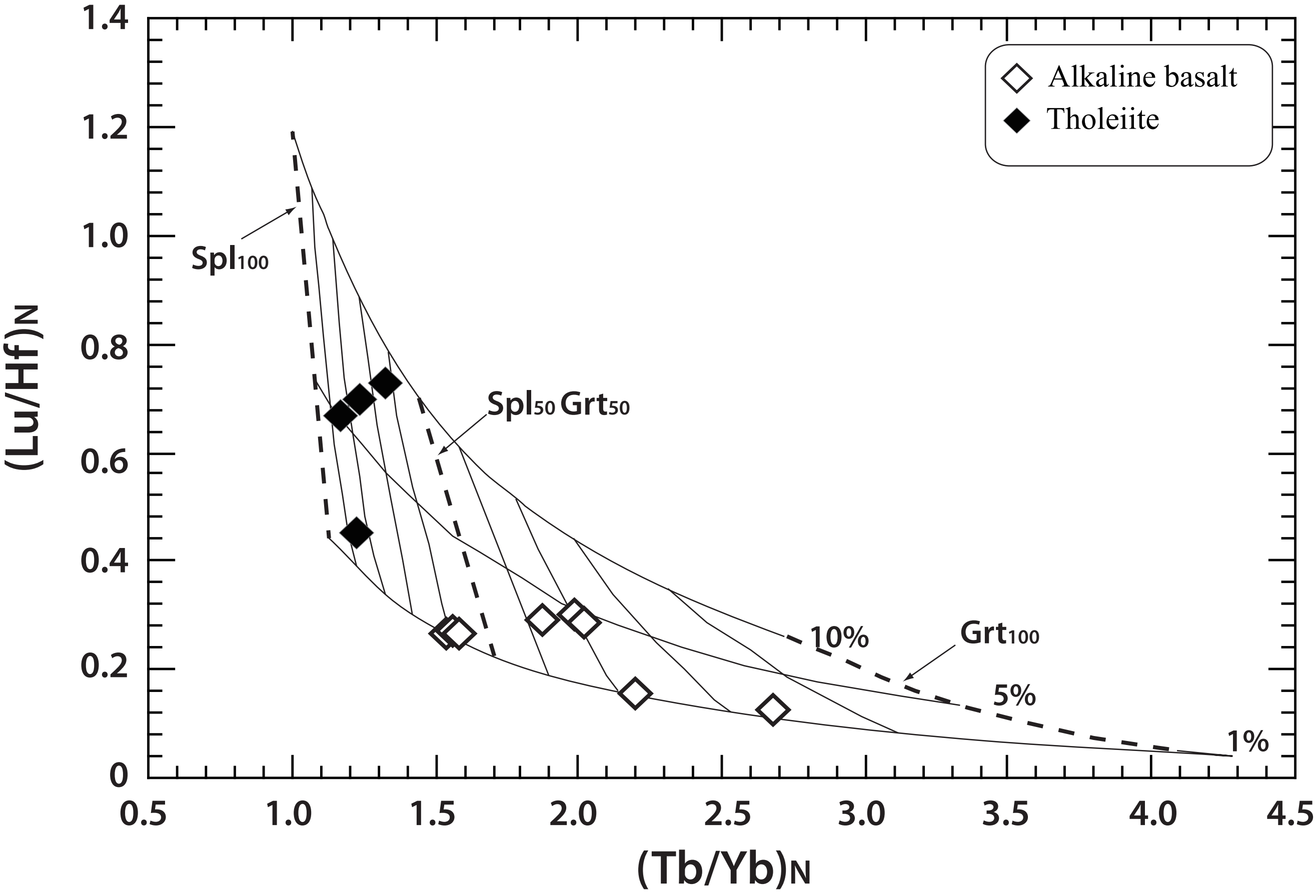

1.4
1.2
1.0
0.8
0.6
0.4
0.2
0
(Lu/Hf)N
0.5
1.0
1.5
2.0
2.5
3.0
3.5
4.0
4.5
(Tb/Yb)N
Alkaline basalt
Tholeiite
Spl100
Spl50 Grt50
Grt100
10%
5%
1%

Figure 7

(a)

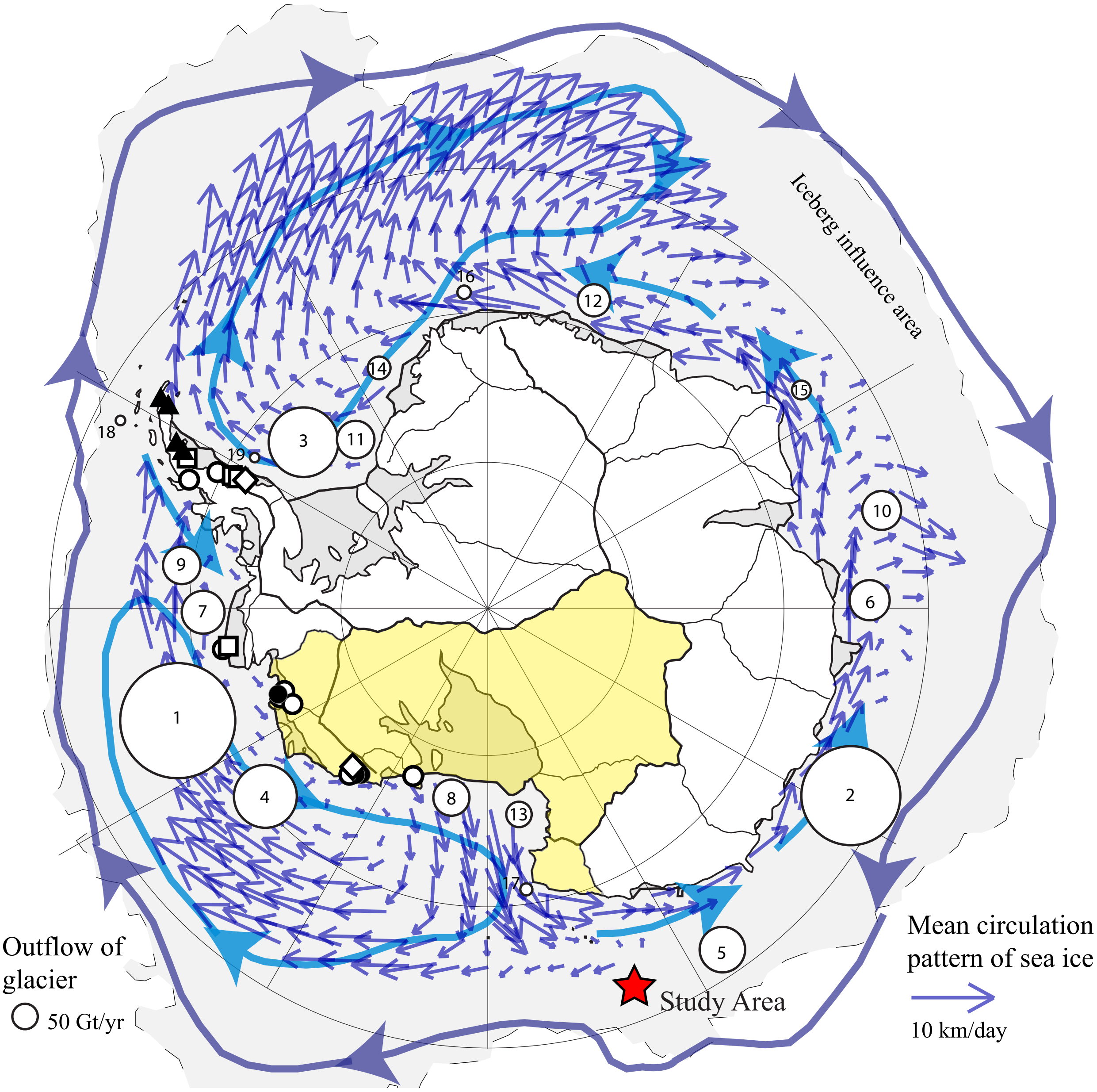
Iceberg influence area
16
12
14
15
3
11
18
19
10
9
6
7
1
2
4
8
13
17
5
Outflow of glacier
50 Gt/yr
Study Area
Mean circulation pattern of sea ice
10 km/day

(b)

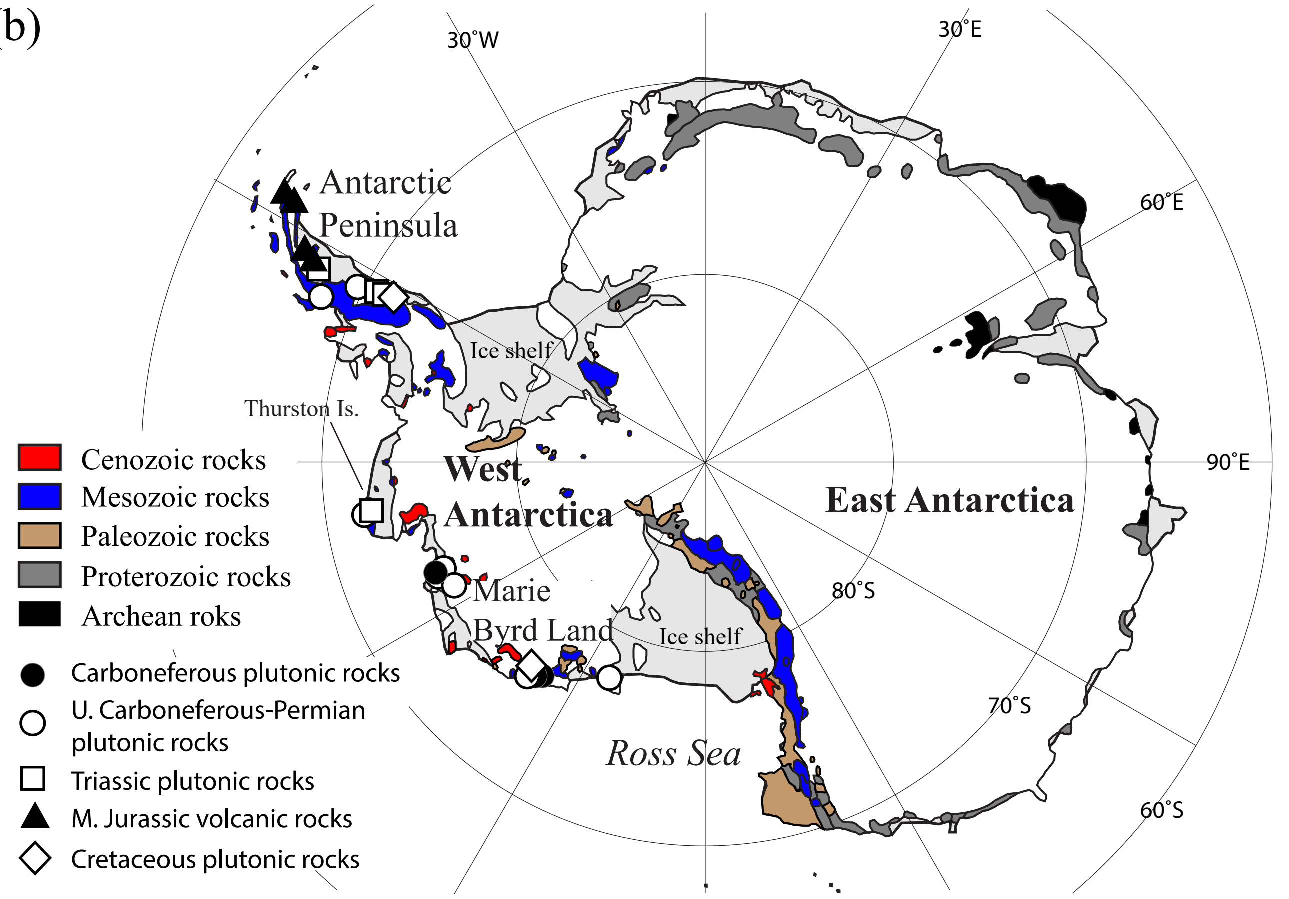
30˚W
30˚E
60˚E
90˚E
80˚S
70˚S
60˚S
Antarctic Peninsula
Ice shelf
Thurston Is.
West Antarctica
East Antarctica
Marie Byrd Land
Ice shelf
Ross Sea
Cenozoic rocks
Mesozoic rocks
Paleozoic rocks
Proterozoic rocks
Archean roks
Carboneferous plutonic rocks
U. Carboneferous-Permian plutonic rocks
Triassic plutonic rocks
M. Jurassic volcanic rocks
Cretaceous plutonic rocks

Figure 8